TU Delft

Delft University of Technology

Document Version
Final published version

Licence
CC BY

Citation (APA)
Aprea, E., Pirim, F., Stallone, F. S., Gkouzioti, V., Liao, Z., Abelmann, L., Frimat, J. P., Sarro, P. M., & Boutry, C. (2026). A biodegradable implantable micropump for biomedical applications, focusing on peripheral nerve repair. *Nano Research*. https://doi.org/10.26599/NR.2026.94908590

Important note
To cite this publication, please use the final published version (if applicable).
Please check the document version above.

Copyright
In case the licence states “Dutch Copyright Act (Article 25fa)”, this publication was made available Green Open Access via the TU Delft Institutional Repository pursuant to Dutch Copyright Act (Article 25fa, the Taverne amendment). This provision does not affect copyright ownership.
Unless copyright is transferred by contract or statute, it remains with the copyright holder.

Sharing and reuse
Other than for strictly personal use, it is not permitted to download, forward or distribute the text or part of it, without the consent of the author(s) and/or copyright holder(s), unless the work is under an open content license such as Creative Commons.

Takedown policy
Please contact us and provide details if you believe this document breaches copyrights.
We will remove access to the work immediately and investigate your claim.

This work is downloaded from Delft University of Technology.

Nano Research

ISSN 1998-0124 CN 11-5974/O4
https://doi.org/10.26599/NR.2026.94908590

Research Article

A biodegradable implantable micropump for biomedical applications, focusing on peripheral nerve repair

Elena Aprea[1], Feyza Pirim-Aslan[1], Francesco Stallone[2], Vasiliki Gkouzioti[3], Zhengwei Liao[1], Leon Abelmann[1], Jean-Philippe Frimat[3], Pasqualina M. Sarro[1], Clementine M. Boutry[1](✉)

[1] Department of Microelectronics, Delft University of Technology, 2628 CD Delft, the Netherlands

[2] Else Kooi Laboratory, Delft University of Technology, 2628 CD Delft, the Netherlands

[3] Department of Neurology and Department of Human Genetics, Leiden University Medical Center, 2333 ZC Leiden, the Netherlands

Nano Res., **Just Accepted Manuscript** • https://doi.org/10.26599/NR.2026.94908590

https://www.sciopen.com/journal/1998-0124 on Feb. 22, 2026

© The Authors(s)

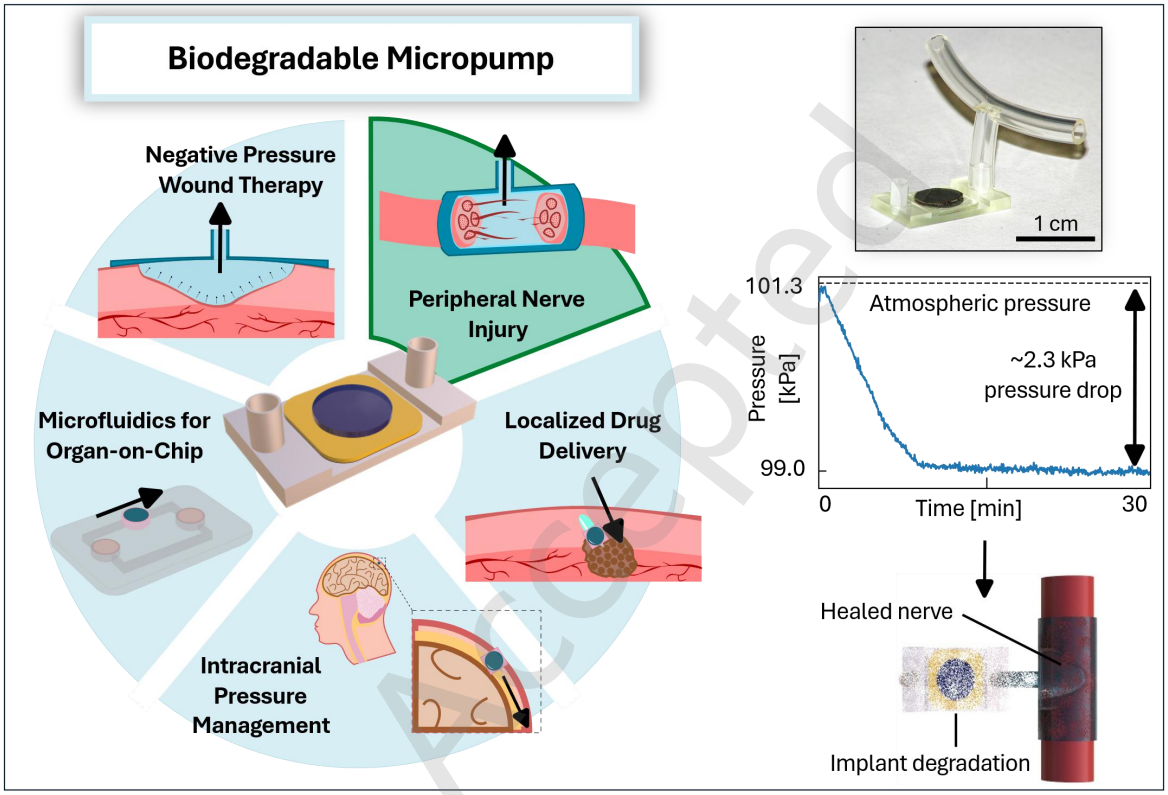
Just Accepted

This is a "Just Accepted" manuscript, which has been examined by the peer-review process and has been accepted for publication. A "Just Accepted" manuscript is published online shortly after its acceptance,which is prior to technical editing and formatting and author proofing. Tsinghua University Press (TUP) provides "Just Accepted" as an optional and free service which allows authors to make their results available to the research community as soon as possible after acceptance. After a manuscript has been technically edited and formatted, and the page proofs have been corrected, it will be removed from the "Just Accepted" web site and published officially with volume and article number (e.g., *Nano Research*, **2025**, *18*, 94906990). Please note that technical editing may introduce minor changes to the manuscript text and/or graphics which may affect the content, and all legal disclaimers that apply to the journal pertain. In no event shall TUP be held responsible for errors or consequences arising from the use of any information contained in these "Just Accepted" manuscripts. To cite this anuscript please use its Digital Object Identifier (DOI®),which is identical for all formats of publication.

Just Accepted

TABLE OF CONTENTS (TOC)

A biodegradable implantable micropump for biomedical applications, focusing on peripheral nerve repair



This work presents the first fully biodegradable, wireless micropump for biomedical implants, made entirely from bioresorbable materials. The device demonstrates stable performance by generating the required under-pressure for applications like peripheral nerve regeneration, while eliminates the necessity of secondary extraction surgery.

Just Accepted

Nano Research

Open Access

Research Article

A biodegradable implantable micropump for biomedical applications, focusing on peripheral nerve repair

Elena Aprea[1], Feyza Pirim-Aslan[1], Francesco Stallone[2], Vasiliki Gkouzioti[3], Zhengwei Liao[1], Leon Abelmann[1], Jean-Philippe Frimat[3], Pasqualina M. Sarro[1], and Clementine M. Boutry[1] ✉

[1] *Department of Microelectronics, Delft University of Technology, 2628 CD Delft, the Netherlands*
[2] *Else Kooi Laboratory, Delft University of Technology, 2628 CD Delft, the Netherlands*
[3] *Department of Neurology and Department of Human Genetics, Leiden University Medical Center, 2333 ZC Leiden, the Netherlands*

Received: 26 November 2025; **Revised:** 13 February 2026; **Accepted:** 22 February 2026

✉ Address correspondence to c.m.f.viellard-boutry@tudelft.nl

Cite this article: *Nano Research*, **2026**, *19*, 94908590. https://doi.org/10.26599/NR.2026.94908590

ABSTRACT: Fully biodegradable microsystems enable therapies for temporary medical conditions that could not be addressed before. We present the first entirely biodegradable, wireless, implantable micropump for biomedical applications, with potential uses ranging from internal negative pressure wound therapy and drug delivery to soft robotics for temporary incontinence. As a proof-of-concept, the micropump was designed for peripheral nerve repair. It is magnetically actuated, featuring a nozzle/diffuser configuration, with a membrane of POMaC elastomer bonded to a magnetic POMaC/CIP composite. POMaC/CIP 20 wt% is selected for its mechanical and magnetic properties (Young's modulus: 45 kPa, magnetic relative permeability: 1.14). A magnetic disc (6 mm x 0.5 mm) maximizes displacement and is actuated via a motor-driven magnetic setup at 4-8 Hz. An equivalent circuit model predicts under-pressure generation trends, confirmed experimentally through continuous/alternate pumping, repeatability assessments, and 240,000-cycle stability tests. *In vitro* and *ex-vivo* tests demonstrate consistent under-pressure (~2.3 kPa), meeting nerve regeneration requirements. Accelerated degradation tests show 31% mass loss after seven weeks, supporting short-term use. This platform is adaptable to diverse biomedical contexts, enabling novel therapies previously unachievable.

KEYWORDS: biodegradable implants, micropump, magnetic actuation, POMaC-CIP composite

Just Accepted

1 Introduction

Biodegradable Micro-Electro-Mechanical Systems (MEMS) represent a new generation of microsystems constructed exclusively from biodegradable materials, including sensors, actuators, and electronic components. Their transient nature enables them to safely dissolve in the body after a defined functional period without the need for surgical retrieval. Here, we present the first fully biodegradable, wireless, implantable micropump designed for biomedical applications [1].

The availability of such a micropump opens new possibilities for temporary medical treatments that were previously unattainable, as illustrated in Figure 1. In surgery, implanting the biodegradable micropump could enable internal negative-pressure wound therapy, extending the established benefits of external vacuum-assisted healing to subcutaneous or deep wounds. The micropump could generate under-pressure by suction at the site of an internal deep wound. By connecting the micropump inlet to the wound through a patch, as done for external wounds, tissue regeneration in internal wounds could be stimulated. This approach promotes granulation tissue formation and infection control, while removing the need for external tubing or device extraction through the transient nature of the biodegradable implant [2-4]. In another context, applying localized under-pressure has been shown to support regeneration after peripheral nerve injury [5]. This technique is especially promising across large gaps (> 1 cm), where conventional microsuturing or autografting techniques are less effective and may cause donor-site morbidity [6-9]. A biodegradable micropump could be a candidate to accelerate nerve regeneration, while being reabsorbed by the body after the treatment is completed. In addition, non-transient implantable, flexible, and wireless micropumps for targeted drug delivery have already proved to be beneficial [10-15]. However, biodegradable alternatives would enable transient drug administration, maintaining delivery only for the required therapeutic period and subsequently degrading naturally, thereby eliminating the need for surgical extraction. This approach could use a micropump to move the drug fluid from a reservoir to the delivery site. Transport would occur through displacement of the main chamber membrane. In another context related to neurosurgery, regulating cerebrospinal fluid using micropumps may improve intracranial pressure management in hydrocephalus. The micropump could be combined with a shunt to displace and drain cerebrospinal fluid from the brain to the abdominal cavity [16, 17]. Controlled under-pressure and biodegradability could address current clinical limitations. This would make the system suitable for transient hydrocephalus and allow adjustable treatment in chronic cases. Finally, another potential application of a biodegradable micropump lies in

organ-on-chip technologies. The need for precise fluid pumping and displacement, coupled with mechanical actuation, is well-established in this field and achieved with (micro)pumps [18, 19]. Employing a biodegradable device would enable more sustainable cell culture practices by reducing reliance on disposable plastics, thereby minimizing environmental impact. The micropump could be integrated into existing microfluidic organ-on-chip platforms, with the scope of controlled circulation of fluids such as cell culture media. Its compact size is comparable to current systems on the market and in research. The actuation could be miniaturized and made wireless, which would replace the bulky, tube-based pumps currently used in incubators. The objective is to develop a proof-of-concept micropump that can serve as a foundational platform for the various applications described above. To establish more specific and coherent design requirements, we have chosen to focus on the nerve repair application. The requisites of the micropump are defined by Sahar *et al.* in their study describing the application of under-pressure within a neural conduit to accelerate the regeneration of a transected nerve following peripheral nerve injury. Our goal is to develop a micropump that could, in various contexts, enable the exploration of new therapeutic approaches that were previously inaccessible.

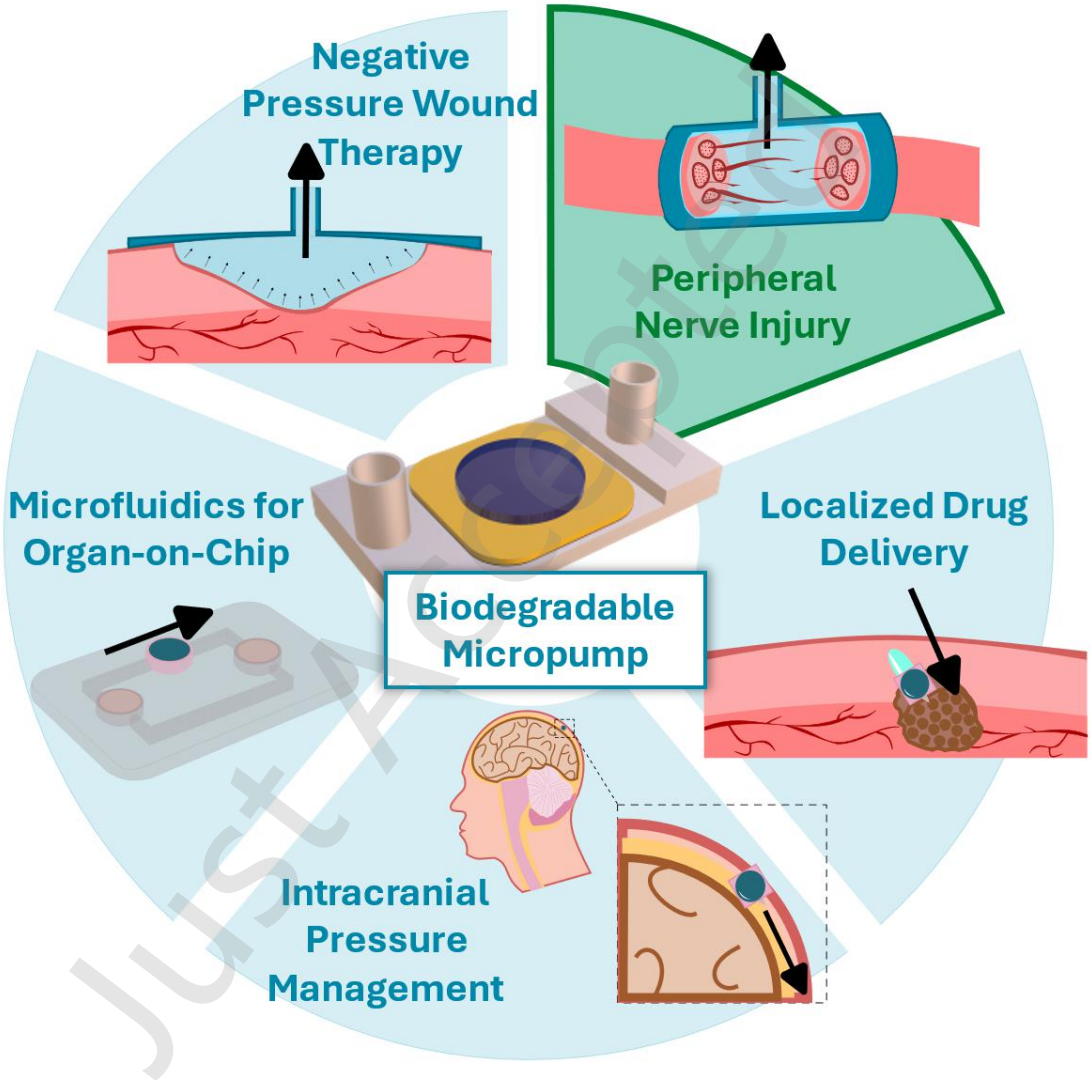


Figure 1 Overview of potential applications of a biodegradable micropump. Examples include: internal negative pressure wound therapy for healing internal lesions; under-pressure generation on a transected nerve to stimulate regrowth (the focus of this work); fluid displacement for localized drug delivery; cerebrospinal fluid displacement to manage intracranial pressure in hydrocephalus; and microfluidic displacement in organ-on-chip systems.

2 Results and discussion

2.1 Micropump Design

Previous studies [5] investigated peripheral nerve repair in rat models using under-pressure and a T-shaped nerve conduit to bridge the transected nerve ends. The conduit was connected to a bulky laboratory vacuum pump positioned externally outside the body. They reported remarkable results, with gross nerve growth improved by a factor of 6. Our goal is to develop a technology that could replace the bulky, wired laboratory pump and enable a realistic clinical application.

To meet the requirements of this specific application, our implantable micropump was designed with the following specifications: 1) It should be able to reach a stable pressure of ~2 kPa below atmospheric level, to comply with optimized results from literature [5]. 2) The target micropump should be flat with a size less than 1 cm^3 to ensure adequate miniaturization and suitability for implantation. 3) The device should operate wirelessly and 4) without a battery, avoiding transcutaneous cables and enabling safer functionality. 5)

Just Accepted

Finally, full biodegradability should be considered a key feature, since non-biodegradable micropumps would require surgical removal, increasing patient risk and discomfort, adding cost to the healthcare system, and potentially damaging internal tissues.

Mechanical micropumps typically rely on piezoelectric or electromagnetic actuation. In this work, magnetic actuation is selected to avoid the high voltages and complex wiring or electronics required in piezoelectric systems. Furthermore, the micropump design employs a nozzle/diffuser valve configuration [20-23], chosen to eliminate both active and passive valves with moving parts, thereby reducing the risk of mechanical failure.

Diffuser elements are constrictions within the fluidic channels that create direction-dependent hydraulic resistance. This causes different flow rates under identical pressure conditions, depending on the flow direction. A diffuser gradually widens along the flow direction, reducing resistance, whereas a nozzle narrows, increasing resistance. In a reciprocating micropump, each nozzle/diffuser element alternates roles during the actuation cycle, acting as a diffuser during one phase and as a nozzle during the other. The cycle includes two modes: (I) a *supply mode*, in which the membrane rises and the chamber volume increases, allowing more fluid to enter through the inlet than exit through the outlet; and (ii) a *pump mode*, in which the membrane lowers and the chamber volume decreases, forcing more fluid through the outlet than through the inlet [23,24].

The valve dimensions are based on established designs from the literature (listed in ST1, Electronic Supplementary Material) [24-26]. To minimize flow losses, diffuser elements with small opening angles are preferred. Previous studies have shown that the optimal diffuser angle is close to $2\theta \approx 11°$ in channels with gradually widening walls [27]. Finite element simulations have been performed to support this result, and are presented in Figure S1 (Electronic Supplementary Material). These findings have guided the selection of the diffuser angle in our design. The diffuser elements have a minimum diameter of a_{min} = 100 µm, a maximum diameter of A_{max} = 500 µm, and a length of l_v = 1130 µm.

Figure 2(a) shows an exploded view of the biodegradable pump and its cross-section, zooming in on the geometry of the outlet diffuser. The first part is the base; it is made from a biodegradable resin (SUNLU), which provides micrometer-level precision for the nozzle/diffuser and microchannels. It is fabricated through the 3D printing using digital light processing technique (curing light wavelength: λ = 405 nm). This method is selected because it enables high-resolution printing and the creation of hollow channels (channel diameter: d_c = 100 µm) quickly and consistently. The nozzle/diffuser elements and a glue reservoir (depth: h_g = 100 µm) are integrated into the printed structure. The T-shaped conduit is connected to the base through the inlet.

The second component is the elastomeric membrane layer, made from Poly(Octamethylene Maleate (Anhydride) Citrate) (POMaC). The elastomer is synthesized and micro-molded into 500 µm-thick layers, then laser-cut to achieve the desired shape (see Experimental Section). POMaC is selected for its biodegradability, biocompatibility, elastomeric properties, and its extended use in biomedical applications, as established in the literature [28, 29].

The third component is the magnetic composite disc, composed of POMaC and Carbonyl Iron Particles (CIP). Its structure is shown in Figure 2(b) using a scanning electron microscope (SEM). This novel composite is created by mixing POMaC with CIP and is synthesized and evaluated in three different weight percentages. The final selection of the POMaC/CIP 20 wt% formulation is based on simulation results and ease of handling (further details are provided later in this section).

The magnetic composite is bonded to the POMaC membrane by UV exposure (365 nm, 225 mW, 2 minutes). The assembled POMaC and POMaC/CIP layers are then attached to the base using a biodegradable surgical fibrin adhesive (TISSEEL) placed in the dedicated reservoir. This glue preserves the overall biodegradability and overall biocompatibility of the device. Figure 2(c) presents a photograph of the complete micropump assembly, including its connection to the T-shaped conduit.

Alternating magnetic fields are used as the driving mechanism to enable wireless actuation. These fields are known to be transparent to the human body, offering a safe and non-invasive method to displace the pump membrane [30]. Biological tissues exhibit very low magnetic susceptibility, as evidenced by the routine clinical use of MRI, where magnetic fields several orders of magnitude higher than those used here are applied without adverse neural effects [31–34]. Similarly, magnetic hyperthermia therapies employ comparable field amplitudes at much higher frequencies without direct interference with neural signaling [35–37]. Although proteins containing iron are present in the body, their weak magnetic response does not lead to significant interactions under low frequency, low amplitude magnetic exposure [38–40]. The micropump is operated by a setup external to the human body that controls it wirelessly. The setup comprises a single diametrically magnetized ring magnet (outer diameter: 26 mm) mounted on a motor rotating at 2, 3, and 4 Hz. When the motor rotates at f_{motor} = 4 Hz, the micropump membrane oscillates at $f_{membrane}$ = 8 Hz. The membrane is periodically attracted to the magnet, depending on the orientation of its magnetic poles relative to the magnetic disc.

Figure 2(d) shows the performance of the micropump during continuous actuation for 30 minutes under an alternating magnetic field (field: B = 0-150 mT, $f_{membrane}$ = 8 Hz). The pump-magnet distance is d_{PM} = 10 mm. The net pressure drop below the atmosphere is $\Delta P \approx$ 2.3 kPa, obtained ~10 minutes after the start of the actuation. This value falls within the target under-pressure range of 1.3 to 2.6 kPa defined by literature [5], demonstrating that the design meets the specified performance criteria.

Not Accepted

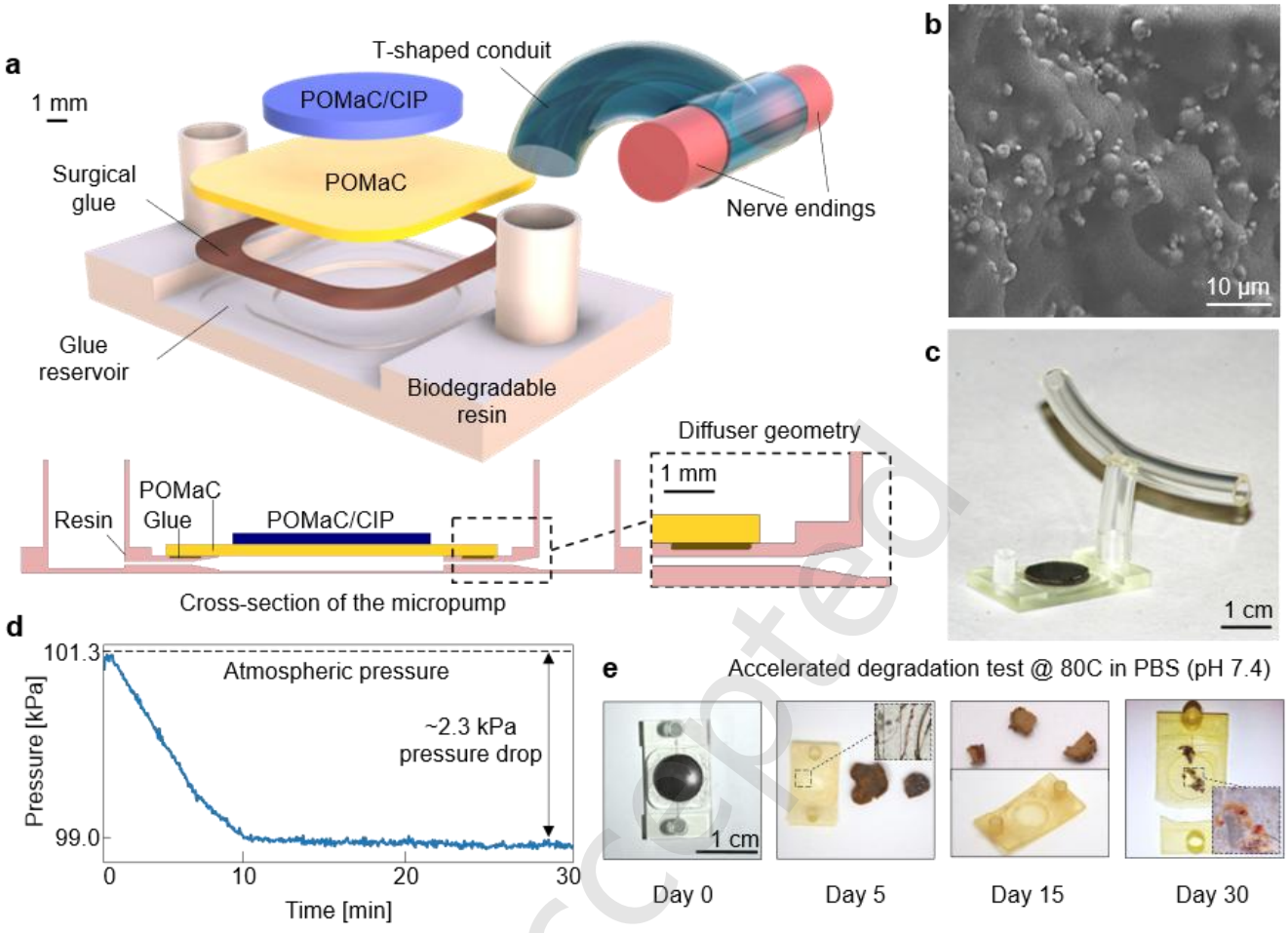


Figure 2 A biodegradable implantable micropump for various biomedical applications. It is designed here to meet the specific requirements of peripheral nerve repair. a) Exploded and cross-sectional views showing the nozzle/diffuser micropump structure: a 3D printed biodegradable base with integrated glue reservoir, surgical glue layer, elastomeric POMaC membrane, and a ferromagnetic POMaC/CIP composite disc. Inset: focus on outlet nozzle/diffuser geometry. b) SEM image of the POMaC/CIP 20 wt% composite for magnetic actuation. c) Fully assembled micropump integrated with a T-shaped conduit to anchor nerve stumps without tension. d) Under-pressure performance under alternating magnetic field for 30 minutes (B = 0–150 mT, $f_{membrane}$ = 8, d_{PM} = 10 mm), reaching a pressure drop of $\Delta P \approx 2.3$ kPa after 10 minutes. e) Accelerated degradation test in PBS at 80 °C showing progressive micropump erosion: membrane detachment by day 5, POMaC degradation by day 15, and substantial resin cracking by day 30.

One of the key features of the device is the biodegradability of its components. Previous studies have demonstrated that in phosphate-buffered saline (PBS) at 37 °C, POMaC shows a layer-by-layer degradation rate of approximately 7–8% mass loss per week [29], while iron foils degrade at about 80 nm per day [41]. Surgical glue is reabsorbed by the body within 2 weeks [42]. However, studies including the characterization of the biodegradable resin's degradation are missing.

In the implanted device, however, not all components are equally exposed to body fluids. External surfaces experience direct exposure, whereas other components remain partially shielded, leading to spatially heterogeneous degradation. Thus, material-level degradation rates reported in the literature cannot be directly extrapolated to the assembled system. The degradation behavior of the micropump is therefore intrinsically coupled to its design; the overall geometry, including thickness, size, and surface-to-volume ratio, can be tailored to the implantation site. Moreover, higher exposed surface areas correspond to accelerated degradation. Structural architecture also plays a critical role. For a given shape, solid structures degrade more slowly than partially hollow designs. Hollow devices can be used to accelerate degradation while reducing material usage and device mass, which may be advantageous for applications requiring rapid resorption. Finally, the dominant erosion mechanism, surface or bulk erosion, depends on both the implantation environment and the selected material, as local physiological conditions such as pH and fluid exchange can vary across implantation sites and influence degradation pathways.

In order to analyze a representative degradation behavior of the device, an accelerated test is conducted in PBS (pH 7.4) at 80 °C, as illustrated in Figure 2(e). Day 0 represents the initial condition of the micropump. By day 5, POMaC and POMaC/CIP components detach from the base due to degradation of the surgical glue. POMaC shows a yellow color, while POMaC/CIP undergoes visible oxidation, and the 3D-printed resin begins to form surface cracks. By day 15, POMaC is completely dissolved. Only small remnants of the composite are left. By day 30, these remnants are minimal, and the resin is

Just Accepted

severely eroded, brittle, and fractured into two pieces. To ensure proper operation of the device over the period of interest, it is relevant to consider packaging, to protect active components, and design choices that account for material thickness and degradation profiles. For a given application and local environment, including pH and fluid exposure, performance must be tested in physiologically relevant environments. In this work, the micropump is tested in PBS at 37 °C as well, to confirm the degradability of the device in human body-like conditions. It shows less than 2.2% mass loss and no structural damage after two weeks, matching the target operational timeframe for peripheral nerve regeneration reported in literature [5]. While a degradation at 80 °C provides a mass loss of 31% after 7 weeks, a degradation at 37 °C provides a mass loss of 10% after 7 weeks. Further explanation of the tests is available in Figure S2 (Electronic Supplementary Material).

2.2 POMaC/CIP Synthesis and Characterization

The synthesis of the POMaC pre-polymer follows established procedures from the literature [29], as illustrated in Figure 2(a, top). 1,8-Octanediol, citric acid, and maleic anhydride (in a molar ratio of 5:1:4) are mixed at 140 °C for 3 hours under a nitrogen flow to perform a polycondensation reaction. The resulting product is then precipitated in deionized water and dried overnight under nitrogen flow. Figure 3(a, bottom) illustrates the preparation of the POMaC/CIP composite. Porogen, photoinitiator, and CIP particles (1–10 μm in diameter) are added to the POMaC pre-polymer and mixed at 60 °C for 6 minutes. The composite is then cured using a combination of UV irradiation (365 nm, 225 mW) and thermal post-polymerization in an oven at 80 °C. Further details are available in the Experimental Section and Figures S3 and S4 (Electronic Supplementary Material). Three composites are prepared by adding CIP at different weight concentrations: 10 wt%, 20 wt%, and 40 wt%. The structure of the composite is displayed in Figure 3(b), which presents SEM images of POMaC/CIP at 10 wt% (left), 20 wt% (center), and 40 wt% (right).

A systematic study of UV irradiation and oven post-polymerization time is essential to ensure reproducibility across different batches. Table 1 presents the optimized curing times (n = 3 samples for each material). Exposure to UV light induces photo-crosslinking via free-radical polymerization of the vinyl groups. Subsequent oven crosslinking occurs through the free functional groups of citric acid, resulting in ester bond formation within the photo-crosslinked POMaC [43]. Short UV curing times combined with longer oven baking times are used to produce softer and more stretchable materials. The observed trend indicates that increasing the concentration of CIP in the composite results in faster crosslinking times both under UV irradiation and during oven post-polymerization. This is attributed to the reduced amount of elastomeric matrix in the composite. Samples are washed with PBS for 2 minutes to remove porogen and residual debris. Since prolonged PBS soaking can initiate material degradation, the washing time is kept to the minimum required to clean the materials.

Current literature lacks studies on POMaC/CIP magnetic composites; therefore, a detailed characterization of their mechanical and magnetic properties is necessary. Figure 3(c) shows representative stress-strain curves of the materials, obtained using a dynamic mechanical analyzer. The results demonstrate the differences in mechanical behavior between the pure POMaC elastomer and the three composites. The POMaC elastomer exhibits low stress values at high strain levels, while the composites display progressively steeper stress-strain curves as the weight percentage of embedded CIP increases. Young's modulus values are calculated from the elastic region of the curves and are presented in Table 2.

Figure 3(d) presents the magnetization curves for the three composites and pure CIP. The measurements are conducted using a superconducting quantum interference device at 37 °C, with a magnetic field sweep from –1 T to 1 T. The graph shows that saturation magnetization (m_s) increases with higher weight percentages of CIP in the elastomer samples. Pure CIP exhibits a m_s = 200 A m^2 kg^{-1}, according to literature values [44]. For POMaC/CIP composites, the m_s values are 40, 89, and 158 A m^2 kg^{-1} at 10 wt%, 20 wt%, and 40 wt% CIP concentrations, respectively. The amount of CIP significantly influences saturation magnetization; composites with higher CIP concentrations exhibit greater saturation magnetization, consistent with literature findings [44]. Equations 1 and 2 are used to calculate the magnetic permeability (r) of the composites:

$$_{s,n} = \quad , (1)$$

$$= 1 + \quad , (2)$$

where $m_{s,n}$ is the resulting magnetization of the composite normalized to the material density of the materials, H_s is the applied magnetic field at saturation, and is the magnetic susceptibility of the material [45]. The density, Young's modulus, and magnetic relative permeability values of the materials are reported in Table 2.

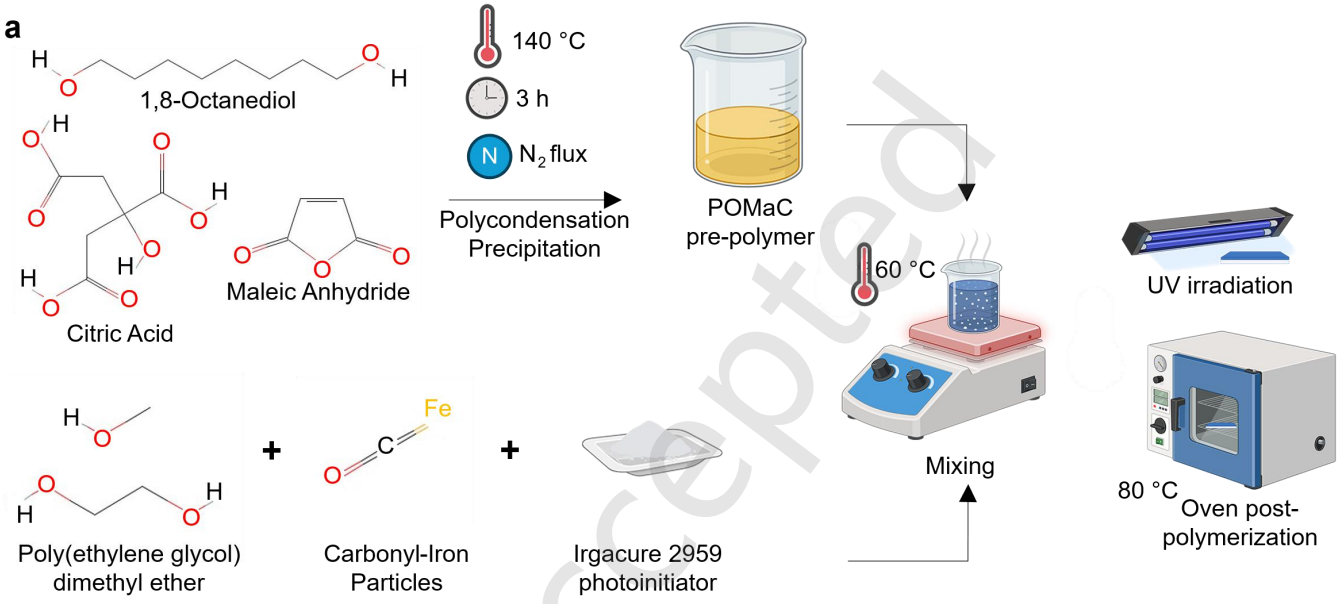
Table 1. Pure elastomer and composites crosslinking study. UV irradiation time (365 nm, 225 mW) and oven post-polymerization time (80 °C).

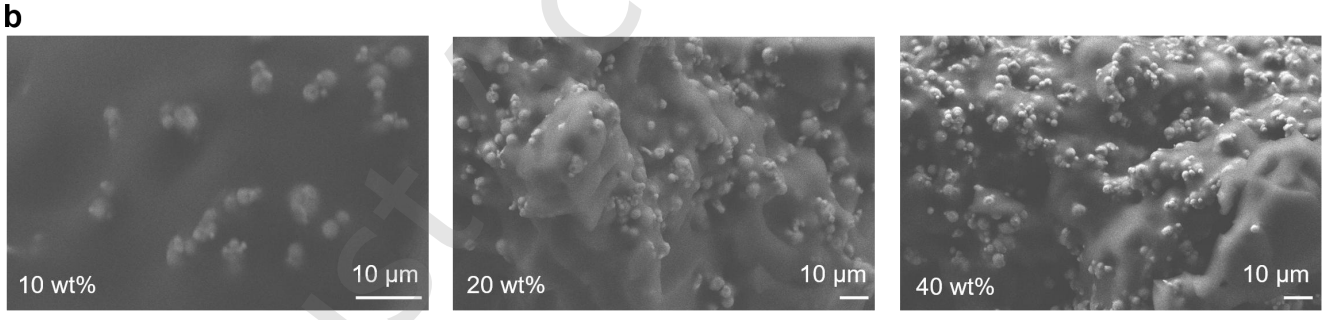
Material	UV time [h:min:s]	Oven time [h:min:s]
Pure POMaC	00:03:00	22:00:00
POMaC/CIP 10 wt%	00:03:30	06:00:00
POMaC/CIP 20 wt%	00:04:15	04:15:00
POMaC/CIP 40 wt%	00:11:00	03:45:00

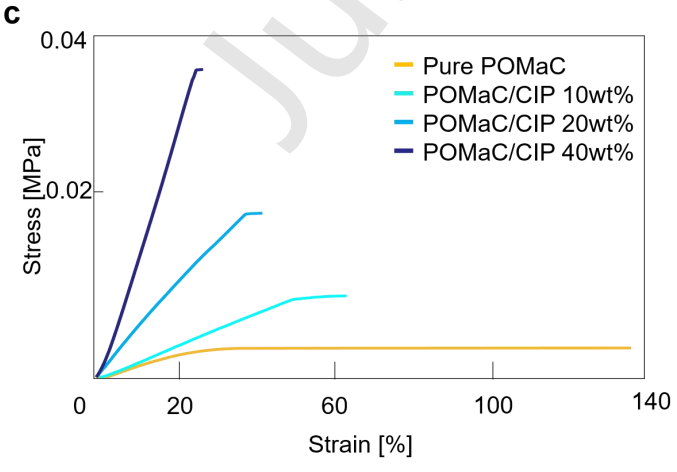
Just Accepted

Table 2. Density and Young's modulus of pure elastomer and composites; magnetic relative permeability of composites.

Material	Density [kg m^{-3}]	Young's modulus [kPa]	Magnetic Relative Permeability [-]
Pure POMaC	726	19.0	-
POMaC/CIP 10 wt%	897	12.5	1.0381
POMaC/CIP 20 wt%	1631	45.0	1.1421
POMaC/CIP 40 wt%	1825	108.6	1.2482







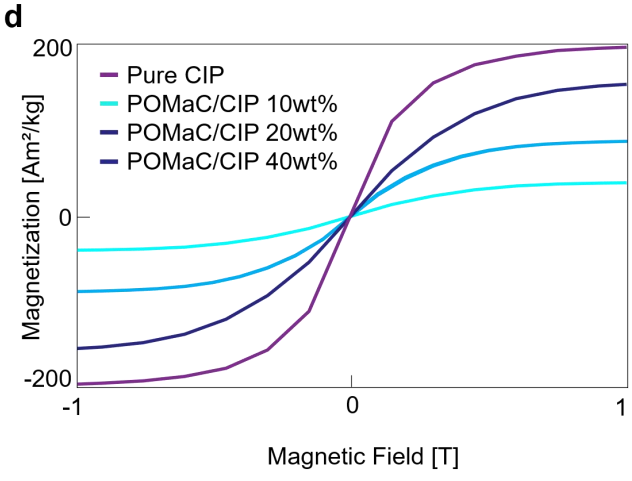


Figure 3 a) Synthesis of the POMaC pre-polymer (top) is carried out via polycondensation of 1,8-octanediol, citric acid, and maleic anhydride in a 5:1:4 molar ratio. The reaction is performed at 140 °C for 3 hours under nitrogen. Fabrication of POMaC/CIP composites (bottom/right) follows by mixing the pre-polymer with porogen, photoinitiator, and CIP (10, 20, and 40 wt%) at 60 °C for 6 minutes. The mixture is then cured under UV light (365 nm) and subjected to oven

Just accepted

polymerization. Partially created with BioRender. b) SEM images of POMaC/CIP composites show CIP particle distribution at concentrations of 10 wt%, 20 wt%, and 40 wt%. c) Stress-strain curves indicate increasing stiffness with higher CIP content. d) Magnetization curves, obtained using a superconducting quantum interference device at 37 °C, show that saturation magnetization increases with CIP concentration. Values reach 40 A m² kg^{-1} for 10 wt%, 89 A m² kg^{-1} for 20 wt%, and A m² kg^{-1} for 40 wt% CIP. Pure CIP exhibits a saturation magnetization of 200 A m² kg^{-1}.

2.3 Finite Element Analysis Simulation

Raising the CIP concentration increases the magnetic relative permeability of the composite but also makes it more brittle. The POMaC/CIP 20 wt% composite exhibits optimal handling properties. Therefore, COMSOL Multiphysics simulations are conducted to evaluate whether it can achieve membrane displacements comparable to those of the 40 wt% composite. The Finite Element Analysis simulations are designed to compare the three composites used for the magnetic part. The goal is to identify which material produces the largest displacement when positioned 10 mm from a magnet (d_{PM} = 10 mm). This distance is selected as it represents a physiologically relevant depth for an implant located beneath the skin [46]. The magnet is a diametrically magnetized ring (NdFeB) with a diameter of 26 mm. Its north pole is oriented perpendicular to the plane of the membrane.

Two membrane designs of the magnetic component are considered. The first design consists of a solid disc ("core") and includes four configurations of outer diameter *(OD*) and thickness (*t*). The second design has a ring-shaped design ("ring") with four configurations of inner diameter (*ID)*, *OD,* and *t* (*ID:OD* ratio: 1:4). The POMaC elastomeric layer of the membrane has a t = 0.5. The *OD, ID,* and *t* of the core and ring configurations are listed in Table ST2 (Supplementary Information). A total of eight configurations is tested.

Young's modulus, density, and specifically for the magnetic composites, relative permeability are adjusted for each material based on the results of the previously described characterization. The analysis is composed of two steps. In the first step, the magnetic field produced by the magnet is evaluated in terms of electromagnetic force applied to the magnetic part of the membrane. In the second step, the force component along the axis perpendicular to the plane of the membrane is applied to the magnetic part of the membrane. The displacement of the membrane across the membrane surface and the volumetric displacement beneath the membrane moving area are evaluated for the three composites (see Experimental Section).

The displacement profiles across the membrane surface for the POMaC/CIP 20 wt% composite are shown in Figure 4(a) for the core design and in Figure S5 (Supplementary Information) for the ring design. The corresponding volumetric displacement values are shown in the bar graphs. For each design, a 3D visualization of the membrane shape is included above the first bar graph to aid in interpretation.

For both designs, configurations with t = 0.2 mm generally produce lower volumetric displacements. In contrast, those with t = 0.5 mm result in higher volumetric displacements and larger displacements across the membrane surface.

Among the core configurations with a t = 0.5 mm, the version with *OD* = 6 mm yields higher volumetric displacement than the one with an *OD* = 4 mm. The increase is 5.6% for the 20 wt% composite and 4.1% for the 40 wt% composite. Among the ring configurations, the combination of *OD* = 4 mm, *ID* = 1 mm, and t = 0.5 mm results in the largest volumetric displacement and displacement profile across the membrane surface.

Overall, the highest volumetric displacement values for each composite are achieved in the two core configurations with a t = 0.5 mm. Among these, the Core 4 membrane configuration is selected as the optimal version because it produces large volumetric displacements, even with the POMaC/CIP 20 wt% composite.

Additional simulations are performed to study how membrane displacement changes with variations in the magnet's distance and the membrane's tilt relative to the magnetic field. Figure 4(b) shows the change in volumetric displacement when the membrane is positioned at d_{PM} = 20 mm from the magnet edge. As expected, the volumetric displacement decreases to 8-10% of the initial values observed at d_{PM} = 10 mm. This trend is observed for all the POMaC/CIP weight concentrations. This highlights the importance of properly securing the micropump within the body after implantation to ensure adequate performance. Figure 4(c) shows the effect of membrane tilt on volumetric displacement for all POMaC/CIP weight concentrations. The tilting angles taken into account are α = 15° along the y-axis of the membrane and β = 15° along the x-axis of the membrane. Tilting the membrane along the y-axis does not impair actuation; instead, it leads to a 7% increase in volumetric displacement for the POMaC/CIP 20 wt% composite. In contrast, tilting the membrane along the x-axis reduces actuation efficiency, with a decrease of approximately 30% at a 15° angular misalignment.

Just Accepted

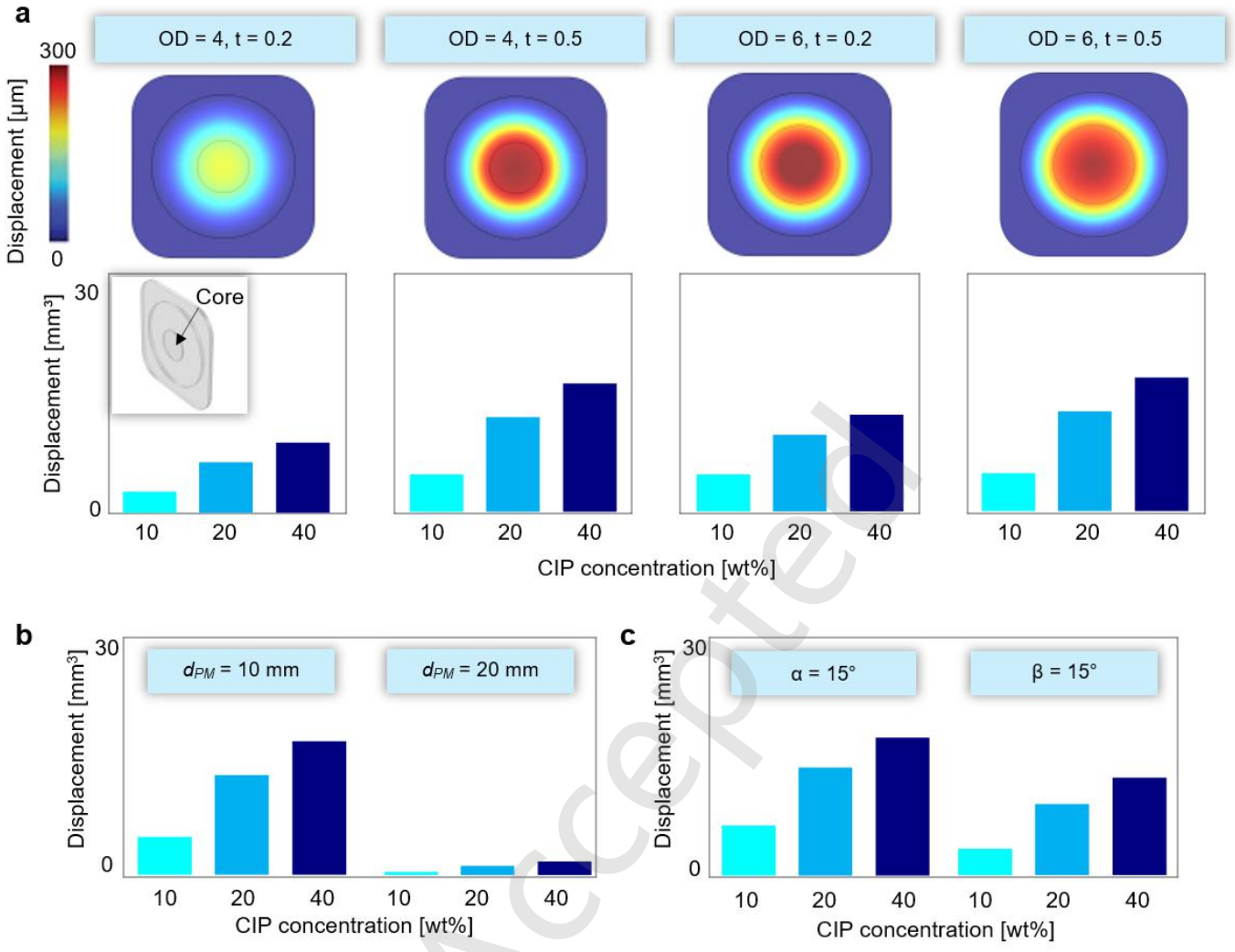


Figure 4 COMSOL Multiphysics simulations comparing membrane displacement across different composite configurations and magnet parameters. Simulations include the three composite types (10, 20, and 40 wt% of CIP), with magnetic and mechanical properties derived from material characterization. The core configuration with POMaC/CIP 20 wt%, *OD* = 6 mm, and *t* = 0.5 mm is selected as optimal for subsequent analysis. a) Representative 3D image, volumetric displacement, and displacement profiles for the core design with varying diameters (*OD* = 4 or 6 mm) and thicknesses (*t* = 0.2 or 0.5 mm), showing increased displacement with thicker and larger magnetic cores. b) Effect of increasing the pump–magnet distance (d_{PM} = 20 mm) on volumetric displacement, showing a drop to 8-10% across all composite types. c) Impact of membrane 15° tilt on displacement, while a rotation along the y-axis does not affect the overall volumetric displacement, a rotation along the x-axis exhibits a decrease in actuation efficiency.

2.4 Micropump Characterization

COMSOL Multiphysics simulations indicate that the membrane design with a core magnetic disc (*OD* = 6 mm, *t* = 0.5 mm) maximizes the displacement. This design allows the use of POMaC/CIP 20 wt%, as it achieves displacement values comparable to those obtained with POMaC/CIP 40 wt%. Therefore, this configuration is selected for fabrication. To verify if the actual displacement of the finalized membrane under a magnetic field matches the simulation results, experimental characterization is performed. A confocal optical sensor is used for this measurement.

Figure 5(a) shows the membrane displacement when placed next to the magnet at distances d_{PM} = 10 mm (top) and d_{PM} = 20 mm (bottom). The light blue rectangles in both subplots highlight the membrane displacement when the ring magnet is positioned next to the membrane with its North pole oriented parallel to the membrane plane. In this case, the magnetic field measured at the membrane site is 0 mT (or below the detection limit of the measuring instrument).

Due to the ferromagnetic behavior of the POMaC/CIP composite, the membrane experiences an alternating magnetic field at twice the motor rotation frequency. When the motor rotates at f_{motor} = 4 Hz, the frequency of the alternating magnetic field applied to the membrane doubles to 8 Hz. When the North and South poles of the magnet are aligned perpendicular to the membrane plane, the magnetic field measured at the membrane site is approximately ±150 mT.

As predicted by simulation for the POMaC/CIP 20 wt% formulation and the selected membrane design, a magnetic field applied at d_{PM} = 10 mm results in a central membrane displacement of approximately 250 µm. When the magnet distance is increased to d_{PM} = 20 mm, the displacement reduces by a factor of 25, confirming the strong dependence on the proximity of the magnetic field.

To better understand the pump's under-pressure output the device is modeled using an equivalent circuit [20, 25, 37]. Analogies between mechanical fluidic systems and electrical circuits are shown in Figure 5(b). Fluidic resistance, capacitance, and impedance are modeled using electrical components: resistors (R), capacitors (C), and inductors (L), respectively. In this analogy, pressure is equivalent to voltage (V). Atmospheric pressure serves as the ground in the equivalent circuit. The tissue

Just Accepted

placed at the inlet, representing the nerve, is modeled with a parallel of equivalent resistance and capacitance. The resistance is analogous to the damping coefficient, and the capacitance to the spring constant, according to the Kelvin-Voigt model [47, 48]. The tubing connecting the micropump to the sensor and the inlet microchannel can be modeled as two RLC circuits. The inlet diffuser is represented by a parallel configuration of resistance, inductance, and two diodes oriented in opposite directions to simulate the directional flow behavior of a diffuser valve [49]. The outlet diffuser valve is represented using the same configuration. R, L, and C are calculated based on the literature [25, 45, 49]. Finally, the outlet is modeled as an RLC circuit, in which the hydraulic resistance, inductance, and capacitance represent the fluidic properties of a large tube, analogous to a body cavity significantly larger than the channels. Actuation is modeled by a sinusoidal voltage, representing the pressure changes in the main chamber due to the membrane displacement. At maximum displacement, the internal pressure drops by approximately $\Delta P_{chamber}$ = 50 kPa relative to the initial atmospheric pressure of 101.3 kPa. $\Delta P_{chamber}$ varies over time depending on the membrane displacement. In the equivalent circuit, it is modeled as a sinusoidal voltage ($V_{chamber}$) with peak amplitude V_p = -1 V and frequency $f_{membrane}$ = 8 Hz. The amplitude value is defined based on the pressure change inside the chamber when the membrane is at its maximum deflection. The selected frequency matches the membrane actuation frequency used in the experimental setup. When the input is applied, the voltage difference between the RLC network representing the tubing and the RC circuit representing the tissue. This difference models the pressure drop in the T-shaped conduit. As shown in Figure 5(c), the curve stabilizes at –27.3 mV after approximately 15 minutes, corresponding to $\Delta P \approx$ -1.36 kPa. This value aligns with the order of magnitude of experimentally measured pressure drops, indicating that the circuit accurately captures the overall trend of the pressure drop dynamics.

More details on the calculations and equivalent circuit components can be found in the Electronic Supplementary Material.

Figure 5(d) shows the setup employed to measure the pressure drop of the micropump: a pressure sensor is connected to the inlet of the micropump. The micropump is positioned at d_{PM} = 10 mm from the magnet, and the pressure drop is recorded over time. Figure 5(e) illustrates the micropump's performance as a function of the number of cycles. Each cycle corresponds to a complete pumping sequence, which includes both the supply and pump phases. A cycle is defined by a full upward and downward movement of the membrane. At a membrane frequency of 8 Hz, the measurement is conducted over 240,000 cycles (corresponding to approximately 500 minutes). The inset highlights the initial 15 minutes of operation, during which the micropump generates an under-pressure that reaches approximately 90 kPa before stabilizing. The full graph confirms consistent and stable operation over the entire testing period. A specific characterization of membrane displacement during long-term actuation (1 week) is provided in the Electronic Supplementary Material (Figures S6 and S7).

Figure 5(f) shows the characterization of the micropump's repeatability. The graph presents three pressure drop curves measured at $f_{membrane}$ of 8, 6, and 4 Hz, all using the same pump. These frequencies are selected because they fall within the operational range of both the micropump and the rotating motor. The pumping becomes unstable at $f_{membrane}$ < 4 Hz, while the current setup limits the f_{motor} to a maximum of 5 Hz. For each frequency, the measurement is conducted over a 30-minute interval. Following each interval, the pressure sensor is disconnected and reconnected, and membrane actuation is resumed after a 30-second stabilization period. The initial stabilization phases are indicated by green rectangles in the graph. For each frequency, the under-pressure level is averaged over the three repetitions. The results obtained show that, at $f_{membrane}$ of 8, 6, and 4 Hz, the under-pressure levels observed are 99.12 ± 0.04, 99.44 ± 0.02, and 99.66 ± 0.07 kPa. These findings demonstrate the repeatability of the system at each actuation frequency.

A follow-up study is conducted to quantify the pump's performance during continuous operation. Figure 5(g) shows the performance of a representative micropump at $f_{membrane}$ equal to 8, 6, and 4 Hz. The micropump shows a consistent trend in under-pressure generation throughout the 30-minute measurement period. An initial pressure drop from atmospheric pressure is followed by stabilization at 99.15 ± 0.10, 99.40 ± 0.02, and 99.65 ± 0.14 kPa for 8, 6, and 4 Hz, respectively. The initial pressure drop follows a linear trend with two distinct slopes: s_A from 0 to 5 min, and $s_{stabilization}$ from 5 minutes to stabilization time. The value of s_A at $f_{membrane}$ equal to 6 Hz and 4 Hz is 32.6% and 44.8% lower, respectively, compared to that at 8 Hz. Similarly, the $s_{stabilization}$ at 6 Hz and 4 Hz is reduced by 20.8% and 54.4%, respectively, relative to the value at 8 Hz.

Overall, higher frequencies lead to a faster and more efficient pressure drop, with $f_{membrane}$ = 8 Hz demonstrating the best performance. The actuation generates an under-pressure $\Delta P \approx$ 2.3 kPa, which satisfies the requirement established by literature [5].

To further evaluate the micropump's performance, a similar experiment is conducted using alternate pumping, as shown in Figure 5(h). After a 30-second stabilization period at atmospheric pressure (green rectangle), the motor is actuated for 5 minutes (Actuation ON). It is then stopped for 5 minutes (Actuation OFF, red background), and this cycle is repeated until the end of the 30-minute measurement. The experiment is performed using three micropumps, with one representative curve shown in the graph. This experiment aims to verify that alternate actuation can achieve the same pressure drop as continuous operation, without significant leakage during the "OFF" periods. The pressure drops stabilize at 99.03 ± 0.06, 99.41 ± 0.02, and 99.60 ± 0.02 kPa for 8, 6 and 4 Hz, respectively. This result is also consistent with the findings from the continuous pumping experiment. The measurements show a pressure drop characterized by two main slopes for each experiment: s_A from 0 to 5 minutes, and s_B from 10 to 15 minutes. The value of s_A at $f_{membrane}$ equal to 6 and 4 Hz is 31.8% and 49.5% lower, respectively, compared to that at $f_{membrane}$ = 8 Hz. This shows good agreement with the continuous pumping experiment. The value of s_B at $f_{membrane}$ equal to 6 and 4 Hz is 7.3% and 23.6% less compared to s_B at $f_{membrane}$ = 8 Hz. This is explained by the fact that s_B does not reach the stabilization point of the curve, as it only accounts for the second phase of the Actuation ON period. A bar graph showing the pressure drop slopes for continuous and alternate pumping experiments is reported in Figure 5(I). Negative values are shown as absolute values (plotted as positive) for clarity.

Just Accepted

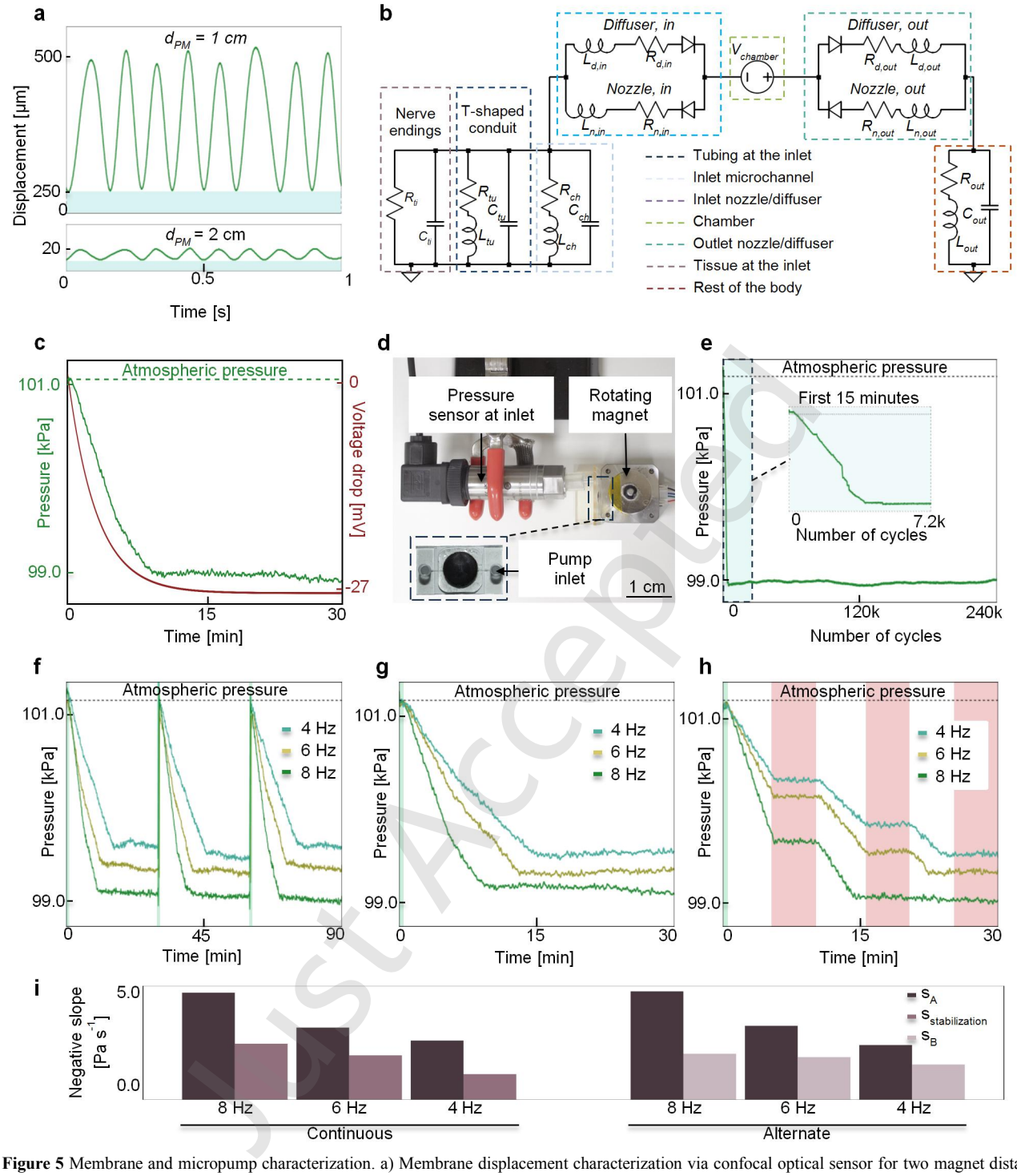


Figure 5 Membrane and micropump characterization. a) Membrane displacement characterization via confocal optical sensor for two magnet distances (d_{PM} = 10 mm and 20 mm), confirming good agreement with finite element analysis simulations. b) Equivalent circuit of the micropump, including an RC configuration representing the tissue, an RLC for the tubing connecting it to the sensor, an RLC for the microchannel, two parallels of R, L, and diodes modeling the nozzle/diffuser configurations at inlet and outlet, and an RLC representing the outlet to the body. $V_{chamber}$ represents the pressure variations in the chamber. c) Comparison between an experimental pressure drop and the output from the model when the actuation frequency is 8 Hz. The equivalent circuit is probed between the RC representing the tissue and the inlet nozzle/diffuser circuit. d) Experimental setup for pressure measurements using a rotating magnet and a pressure sensor. e) Micropump performance over 240,000 cycles (500 min) at 8 Hz actuation shows stable under-pressure generation. Inset: zoom on the initial 15 min. f) Repeatability analysis at three actuation frequencies (8, 6, 4 Hz) over subsequent actuation shows consistent performance for the same actuation frequency, with overall pressure variations below ± 0.1 kPa. g) Continuous actuation tests for 30 minutes at 8, 6, and 4 Hz confirm similar pressure drop trends and stabilization behavior, with higher frequencies achieving faster actuation. h) Alternate actuation test for 30 minutes at 8, 6, and 4 Hz (5 minutes ON/OFF cycles) produces comparable under-pressure trends, indicating reliable and repeatable performance across different operating modes. i) Bar graph showing the pressure drop slopes. Negative values are shown as absolute values (plotted as positive) for clarity. From 0 to 5 minutes (s_A) and from 5 minutes to stabilization ($s_{stabilization}$) at $f_{membrane}$ = 8, 6, and 4 Hz in continuous pumping condition. From 0 to 5 minutes (s_A) and from 10 to 15 minutes (s_B) at $f_{membrane}$ = 8, 6 and 4 Hz in alternate pumping condition.

Just Accepted

2.5 Micropump Testing – Nerve Phantom and *Ex-Vivo*

The micropump is tested in two configurations that replicate the implant setup. It is connected to a nerve phantom and an *ex-vivo* chicken tissue via a T-shaped conduit. In both cases, the same continuous pumping and alternate pumping experiments are performed, to verify a similar behavior of the pump. Consistent with the initial characterization, the pressure drops follow linear trends that can be described using two distinct slopes. In continuous pumping: s_A from 0 to 5 minutes, and $s_{stabilization}$ from 5 minutes to the stabilization point. In alternate pumping: s_A from 0 to 5 minutes, and s_B from 10 to 15 minutes. All the experiments are performed using three micropumps, with one representative curve shown in the graph. All the results are averaged across the three micropumps. During clinical treatment, due to neural regeneration, changes in the volume of the T-shaped conduit subjected to under-pressure may influence the pump operation over time. An interesting direction for future research would be to evaluate a predictive model of nerve regeneration rate, to adjust the external excitation driving the micropump during treatment, or to incorporate a sensor for feedback loop control.

Figure 6(a) presents the experimental setup in which the micropump is connected to the phantom. The same pressure sensor and rotating magnet used in previous experiments are employed in this setup. The micropump's inlet is connected to a T-shaped conduit with an inner diameter of 1.5 mm. The pressure sensor is attached through an opening on the side opposite the micropump. Two Polydimethylsiloxane (PDMS) nerve phantom stumps are inserted into the longer segment of the conduit and secured with surgical glue. They are positioned to leave a 4 cm gap, simulating a peripheral nerve lesion greater than 3 cm.

As shown in Figure 6(b), continuous pumping over 30 minutes at $f_{membrane}$ = 8, 6, and 4 Hz results in an initial pressure drop from atmospheric pressure, followed by stabilization at 99.13 ± 0.08, 99.48 ± 0.07, and 99.69 ± 0.08 kPa. The under-pressure levels show good agreement with those obtained during the continuous pumping characterization conducted without the nerve phantom. The values of s_A and $s_{stabilization}$ in the phantom experiment are 10.7% and 7.6% lower, respectively, compared to those observed in the initial characterization. This difference is likely due to the larger volume of gas that must be displaced initially from the T-shaped conduit. The value of s_A at $f_{membrane}$ equal to 6 and 4 Hz is 30.6% and 47.8% lower, respectively, compared to that at $f_{membrane}$ = 8 Hz. The value of $s_{stabilization}$ at $f_{membrane}$ equal to 6 and 4 Hz is 22.1% and 28.1% less compared to $s_{stabilization}$ at $f_{membrane}$ = 8 Hz. These results are in good agreement with those obtained from the continuous pumping experiment conducted during the initial characterization.

The alternate pumping experiment is shown in Figure 6(c). At $f_{membrane}$ = 8, 6, and 4 Hz, results show an initial pressure drop from the atmospheric level, followed by stabilization at 99.03 ± 0.01, 99.41 ± 0.05, and 99.65 ± 0.05 kPa. The value of s_A at $f_{membrane}$ equal to 6 and 4 Hz is 29.2% and 44.5% lower, respectively, compared to that at $f_{membrane}$ = 8 Hz. This shows good agreement with the continuous pumping experiment on the phantom and with the initial characterization. The value of s_B at $f_{membrane}$ equal to 6 and 4 Hz is 21.2% and 37.8% less compared to s_B at $f_{membrane}$ = 8 Hz. These results exhibit the same trend observed in the alternate pumping test from the initial characterization when compared to the corresponding continuous pumping data. However, overall, all the actuation frequencies in the phantom test result in a slower decay and reduced slope values.

Furthermore, the experiments are repeated in an *ex-vivo* setting using two chicken tissues, each approximately 1.5 mm in diameter. The setup from the phantom experiment is reused, with the chicken tissues inserted into the T-shaped conduit, maintaining a 4 cm gap (Figure 6(d)). The tissues are secured in place using surgical glue.

As shown in Figure 6(e), the measurements of the continuous pumping present an initial pressure drop from the atmospheric pressure and a subsequent stabilization phase at 98.98 ± 0.04, 99.48 ± 0.01, and 99.64 ± 0.03 kPa, respectively. The value of s_A at $f_{membrane}$ equal to 6 and 4 Hz is 31.1% and 46.3% lower, respectively, compared to that at $f_{membrane}$ = 8 Hz. The value of $s_{stabilization}$ at $f_{membrane}$ equal to 6 and 4 Hz is 28.7% and 33.9% less compared to $s_{stabilization}$ at $f_{membrane}$ = 8 Hz. The value of s_A at $f_{membrane}$ = 8 Hz is 11.9% lower compared to the one of the phantom testing, indicating a slower initial decay. However, $s_{stabilization}$ at $f_{membrane}$ = 8 Hz is 10.0% higher than the one of the phantom testing. The slower initial decay is likely due to the characteristics of the animal tissues, which, unlike PDMS and polymeric materials, can release debris and droplets when exposed to under-pressure. The under-pressure range investigated in this work, 2 kPa, was based on literature [5] to ensure nerve integrity, as larger under-pressures (up to 8 kPa) were observed to be associated with increased tissue debris at the interface.

Figure 6(f) shows the alternate pumping results when the micropump is used on tissues. A similar under-pressure is achieved with a different actuation modality. The stabilization phase reached 99.10 ± 0.10, 99.52 ± 0.15, and 99.63 ± 0.04 kPa, respectively. The value of s_A at $f_{membrane}$ equal to 6 and 4 Hz is 33.2% and 43.9% lower, respectively, compared to that at $f_{membrane}$ = 8 Hz. These results are in good agreement with the continuous pumping experiments on the phantom, as well as with the initial characterization and the alternate pumping results obtained on the phantom. The value of s_B at $f_{membrane}$ equal to 6 and 4 Hz is 19.6% and 39.9% less compared to s_B at $f_{membrane}$ = 8 Hz.

A bar graph showing the pressure drop slopes for phantom and *ex-vivo* experiment is reported in Figure 6(g). Negative values are shown as absolute values (plotted as positive) for clarity.

Just Accepted

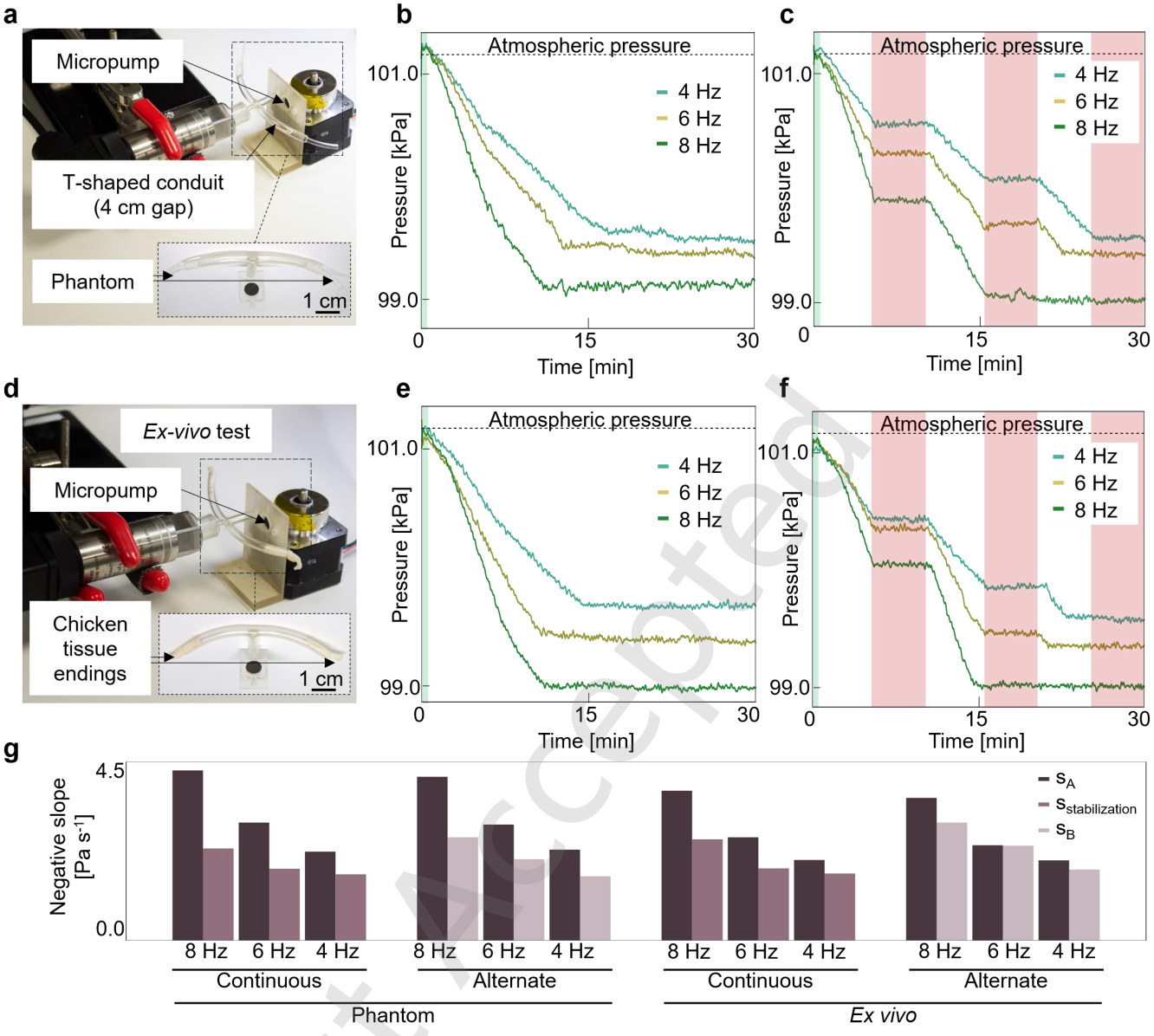


Figure 6 a) Experimental setup for phantom configuration, where the micropump is connected via a T-shaped conduit (1.5 mm inner diameter, 4 cm gap) to a PDMS phantom simulating a peripheral nerve lesion. The setup includes the same pressure sensor and rotating magnet as in previous tests. b) Pressure drop profiles at 8, 6, and 4 Hz obtained from continuous pumping for 30 minutes when the conduit hosts the nerve phantom. c) Pressure drop profiles at 8, 6, and 4 Hz obtained from alternate pumping for 30 minutes when the conduit hosts the nerve phantom. Red background indicates the actuation is OFF. d) *Ex-vivo* configuration using chicken tissues (~1.5 mm diameter) inserted into the conduit and glued in place. The setup used is the same as the one for continuous actuation. e) Pressure drop profiles at 8, 6, and 4 Hz obtained from continuous pumping for 30 minutes when the conduit hosts the chicken tissue. f) Pressure drop profiles at 8, 6, and 4 Hz obtained from alternate pumping for 30 minutes when the conduit hosts the chicken tissues. Red background indicates the actuation is OFF. g) Bar graph showing the pressure drop slopes for phantom and *ex-vivo* experiment. Negative values are shown as absolute values (plotted as positive) for clarity. From 0 to 5 minutes (s_A) and from 5 minutes to stabilization ($s_{stabilization}$) at $f_{membrane}$ = 8, 6 and 4 Hz in continuous pumping condition. From 0 to 5 minutes (s_A) and from 10 to 15 minutes (s_B) at $f_{membrane}$ = 8, 6 and 4 Hz in alternate pumping condition.

3 Conclusion

A novel generation of biodegradable micro-electromechanical systems offers promising solutions to medical challenges that have, until now, remained unresolved. In this work, we present the first fully biodegradable, wireless micropump for biomedical implants, exemplified by its application in peripheral nerve regeneration through localized under-pressure.

The micropump is made from biodegradable resin, surgical glue, POMaC, and a POMaC/CIP magnetic composite, which was optimized using two approaches. Material characterization investigated three CIP ratios (10, 20, 40 wt%) to determine the optimal curing method and assess mechanical and magnetic properties. Finite element analysis guided the selection of the best composite and design for the magnetic element. As a result, the POMaC/CIP 20 wt% composite and a core design were selected (outer diameter of 6 mm, thickness of 0.5 mm).

Micropump characterization demonstrated repeatable pressure profiles under continuous and alternate actuation. Performance remained stable across extended cycles (240,000) and variable frequencies (4, 6, and 8 Hz), confirming the system's reliability. The device was evaluated in clinically relevant settings, including a nerve phantom and an *ex-vivo* tissue model. In both, the micropump produced stable under-pressure. Actuating the micropump membrane *ex-vivo* at 8 Hz generates an under-pressure of 99.10 ± 0.10 kPa in less than 10 minutes. This meets the optimized pressure requirements established by Sahar *et al.*

These results confirm the device's potential as a nerve repair implant and, in general, a biodegradable micropump for temporary usage. Its wireless actuation and full biodegradability solve major drawbacks addressed in the literature, such as transcutaneous implants and secondary extraction surgeries.

By combining magnetic actuation, biodegradability, and microscale fabrication techniques, the system paves the way for

Just Accepted

the development of a new generation of transient biomedical actuators.

4 Experimental Section

Materials: Materials used included Tech Clear resin (Moiin), plant-based resin (SUNLU), surgical glue (TISSEEL), PDMS (Sylgard 184) base and curing agent, 1,8-octanediol, citric acid, maleic anhydride, 1,4-dioxane, poly(ethylene glycol) dimethyl ether (PEGDM) porogen, 2-hydroxy-4′-(2-hydroxyethoxy)-2-methylpropiophenone photoinitiator, carbonyl iron, phosphate buffered saline (PBS), all sourced from Sigma Aldrich unless otherwise specified.

Fabrication of Micropump Base: The base of the micropump was designed on Fusion 360 software and 3D printed with a DLP Asiga Max 3D printer (layer thickness: 50 µm, x-y resolution: 27 µm, z resolution: 50 µm) and plant-based resin.

Synthesis of Pre-POMaC: Pre-POMaC was synthesized by polycondensation reaction of 1,8 octanediol, citric acid, and maleic anhydride (5:1:4) at 140 °C, for 3 hours and under a nitrogen purge. 1 ml of 1-4 dioxane for each gram of chemical product was added to the flask. Pre-POMaC was purified by precipitation in deionized water. The product was dried overnight under a nitrogen purge and stored at 4 °C.

Synthesis of POMaC Magnetic Composite: Pre-POMaC was mixed with PEGDM porogen at a 2:3 weight ratio (POMaC:PEGDM). A 5 wt/vol% photoinitiator was added to the mixture. Three composite formulations were prepared by adding 10 wt%, 20 wt%, and 40 wt% CIP to the POMaC-porogen-photoinitiator mixture. The composites were stirred at 60 °C for 6 minutes to ensure homogeneity.

POMaC and POMaC/CIP Curing and Post-Processing: POMaC and POMaC/CIP composites were cured using a combination of UV curing (DYMAX 5000, 225 mW/cm², 365 nm) and oven post-polymerization at 80 °C. Subsequently, samples were washed in PBS for 2 minutes to remove uncured porogen residues.

Molds Fabrication: Membranes were fabricated by micro-molding POMaC and POMaC/CIP composites. A 180 nm anti-adhesion layer of polytetrafluoroethylene (PTFE) was deposited on a 4-inch, 500 µm-thick silicon wafer using plasma-enhanced chemical vapor deposition (PECVD). The wafer was saw-diced into 2x2 cm² squares and used as master molds for elastomer and composite layers.

A 3 mm-thick PDMS layer was cast on the diced silicon wafer to obtain a negative mold, which was then baked at 80 °C for 2 hours. PECVD was used again to deposit a 180 nm PTFE anti-adhesion layer on the PDMS negative molds. POMaC and POMaC/CIP composites were then cast into these PDMS molds and crosslinked as previously described.

Membrane Fabrication: After crosslinking, 500 µm-thick layers of POMaC and POMaC/CIP were laser cut (CO2 Laser Cutter R400, Trotec) to produce the elastomeric membrane layer and magnetic component, respectively. The layers were aligned and bonded via UV exposure for 2 minutes.

Micropump Assembly: The micropump was assembled using fibrin sealant. Glue was applied to the reservoir of the base, and the membrane (elastomeric layer and magnetic part) was placed on top and allowed to dry.

Characterization of Mechanical Properties: Mechanical properties were measured using a Dynamic Mechanical Analyzer (Q800, TA Instruments). Samples (10 mm x5 mm x 1 mm) were clamped and stretched with 0.001 N preload force and 0.0010% initial strain. The force was increased at a rate of 0.01 N min^{-1} until sample failure. Young's modulus was calculated for each sample.

Characterization of Magnetic Properties: Magnetic properties were measured using a Superconducting Quantum Interference Device (MPMS 5XL, Quantum Design). Samples weighing 2-3 mg were measured. Magnetization curves were obtained by applying a magnetic field sweeping from -1 T to 1 T in 0.1 T increments. Measurements were performed at 37 °C to simulate the physiological environment. Relative permeability was calculated from saturation magnetization values.

Finite Element Analysis simulations: Two membrane designs were modeled: a full disc ("core") and a ring ("ring"), each tested in four configurations. The POMaC base membrane was fixed at the edges with fixed constraints. Material properties were based on prior characterization. The membrane mesh was tetrahedral with *finer distribution*. The model incorporated two physics modules: *Solid Mechanics* and *Magnetic Fields (No Current)*. In the first stationary study, electromagnetic forces from a diametrically magnetized NdFeB magnet were calculated along the direction perpendicular to the membrane using *Global Evaluation.* These forces were then applied in a second stationary study to simulate membrane deformation. Volumetric displacement was determined by surface integration on the free surface opposite the magnet. Displacement plots were exported for analysis.

Custom-made Magnetic Actuation Setup: The magnetic setup consisted of a diametrically magnetized ring magnet (N42, NdFeB, First4Magnets, outer diameter: 26 mm) mounted on a stepper motor (Nema 17). The motor was controlled via an Arduino Uno (Rev 3) and powered by a 12 V power supply (Agilent 6613C DC). A WT10A teslameter (Weite Magnetic Technology Co.) was used to measure the magnetic field at fixed distances from the rotating magnet.

Measurement of Membrane Displacement: The membrane was clamped on a sample holder (3D printed with Tech Clear resin) to guarantee stability and placed at given distances from the rotating magnet. Membrane displacements were recorded using a confocal optical sensor (Microepsilon, confocalDT IFD2411).

Equivalent Circuit Modeling: Values for voltage, resistances, inductances, and capacitances corresponding to the input voltage, tubing, microchannels, and nozzle/diffuser components were calculated as detailed in the Electronic Supplementary Material (ST3). The circuit was modeled using LTSpice.

Measurement of Pressure Drop: The micropump was fixed on a sample holder placed at specified distances from the rotating magnet. Pressure drop characterization was performed by connecting the micropump inlet to a pressure sensor (Druck PTXPRESSX-1; min: 0.8 bar, max: 1.2 bar). N = 3 micropumps were tested at each frequency for the continuous and alternate testing. Phantom experiments involved connecting the inlet of the micropumps (n = 3) to the short part of a T-shaped conduit. The conduit (inner diameter: 1.5 mm, short part: 1 cm, long part: 6 cm) hosted two PDMS (15:1 base:curing agent) tubes of 1.5 mm diameter. The connection with the pressure sensor was located on the other side of the conduit. The same setup and number of micropumps were used for the *ex-vivo* test, with chicken tissue (local butcher) placed in the T-shaped conduit instead of the phantom. Representative curves are shown in the plots. Data were filtered with Butterworth filters (cut-off frequency: 10 Hz) to remove noise. The slope results were averaged among the 3 curves obtained for each frequency. Data analysis on the slope of the pressure drop profiles was performed with OriginPro.

Biodegradability Tests: The biodegradability of the micropump was assessed via accelerated and regular degradation testing, by placing the device in a 7.4 pH PBS solution at 80 °C and 37 °C, respectively. The PBS solution was refreshed every 48 hours, to ensure the same level of acidity throughout the test.

Just Accepted

Electronic Supplementary Material: Supplementary material regarding design, fabrication and modeling is available in the online version of this article at https://doi.org/10.26599/NR.2026.94908590.

Data availability

All data needed to support the conclusions in the paper are presented in the manuscript and/or the Electronic Supplementary Material. Additional data related to this paper may be requested from the corresponding author upon request.

Acknowledgements

E.A. would like to acknowledge Prof. Kaspar Jansen, Prof. Ekkes Brück, Prof. Daniel Pijnappels, Mascha Slingerland, Sebastian Couweleers, Jacques Brenkman, Tim Uliss, the ECTM group, the Else Kooi Laboratory, and the Nerve Repair 2.0 European Research Council (ERC) starting grant. This work was further supported by the Netherlands Organ-on-Chip Initiative, an NWO Gravitation project (024.003.001).

Declaration of competing interest

All the contributing author(s) report(s) no conflict of interests in this work.

Author contribution statement

E.A.: Conceptualization, data curation, formal analysis, investigation, methodology, project administration, supervision, validation, visualization, writing manuscript, experimental design. F.P.A: formal analysis, experimental design. F.S.: investigation, writing (review & editing). V.G.: investigation, writing (review & editing). Z.L: investigation. L.A.: investigation. J.P.F: investigation, writing (review & editing). P.M.S.: resources. C.M.B: conceptualization, project administration, resources, writing (review & editing). All the authors have approved the final manuscript.

Informed consent

Not applicable.

Ethics statement

Not applicable.

Use of AI statement

During the preparation of this work, the author(s) used ChatGPT in order to review grammar and phrasing. After using this tool/service, the author(s) reviewed and edited the content as needed and take(s) full responsibility for the content of the publication.

References

[1] Ganesan K, Palanisamy S, Muthusamy S, Muthusamy PM, Ramamoorthi P, Ravi RK, Sha MS, Sadasivuni KK. A new method for improving the solar photovoltaic unit efficiency through neem oil as coolant medium for high power applications—an experimental investigation. *Electrical Engineering*. **2024** Oct;106(5):6251-64.

[2] Zaver V, Kankanalu P. Negative pressure wound therapy. *InStatPearls [Internet]* **2023** Sep 4. StatPearls Publishing.

[3] Shestak KC. The Internal Negative-Pressure Wound Control System: A Paradigm Shift for Promoting Deep Space Healing in Complex Surgically Created Wounds. *Aesthetic Surgery Journal*. **2021** Nov 1;41(11):NP1543-9.

[4] Miura T, Yamamoto Y, Murao N, Maeda T, Osawa M, Hayashi T, Funayama E. Combined internal and external negative pressure wound therapy: breakthrough treatment for lymphocutaneous intractable fistula. *Surgery Today*. **2021** Oct;51(10):1630-7.

[5] Sahar MS, Mettyas T, Shah M, Bindra R, Barton M. Histological, immunohistochemical, and morphometric analysis of negative pressure-assisted in-vivo nerve stretch-growth. *Neuroscience Letters*. **2022** Jun 21;782:136687.

[6] Schiavone G, Fallegger F, Kang X, Barra B, Vachicouras N, Roussinova E, Furfaro I, Jiguet S, Seáñez I, Borgognon S, Rowald A. Soft, implantable bioelectronic interfaces for translational research. *Advanced Materials*. **2020** Apr;32(17):1906512.

[7] Meena P, Kakkar A, Kumar M, Khatri N, Nagar RK, Singh A, Malhotra P, Shukla M, Saraswat SK, Srivastava S, Datt R. Advances and clinical challenges for translating nerve conduit technology from bench to bed side for peripheral nerve repair. *Cell and tissue research*. **2021** Feb;383(2):617-44.

[8] Rodkey WG, Cabaud HE, McCarroll Jr HR. Neurorrhaphy after loss of a nerve segment: comparison of epineurial suture under tension versus multiple nerve grafts. *The Journal of Hand Surgery*. **1980** Jul 1;5(4):366-71.

[9] Navarro X, Geuna S, Grothe C, Haastert‐Talini K. Introduction: thematic papers issue on peripheral nerve regeneration and repair. The *Anatomical Record*. **2018** Oct;301(10):1614-7.

[10] Gensler H, Sheybani R, Li PY, Mann RL, Meng E. An implantable MEMS micropump system for drug delivery in small animals. *Biomedical microdevices*. **2012** Jun;14(3):483-96.

[11] Bußmann A, Leistner H, Zhou D, Wackerle M, Congar Y, Richter M, Hubbuch J. Piezoelectric silicon micropump for drug delivery applications. *Applied Sciences*. **2021** Aug 30;11(17):8008.

[12] Akram MM, Aghajani A, Shi W, Gosselin B. A closed-loop micropump and flow meter for high-precision drug delivery in an implantable neural probe. *In 2024 46th Annual International Conference of the IEEE Engineering in Medicine and Biology Society (EMBC)* **2024** Jul 15 (pp. 1-4). IEEE.

[13] Mariello M, Eş I, Proctor CM. Soft and flexible bioelectronic micro‐systems for electronically controlled drug delivery. *Advanced Healthcare Materials*. **2024** Sep;13(24):2302969.

[14] Fan Y, Bai R, Chen X, Huang Z, Du N, Nan K. Advances in Flexible Wearable Technologies for Drug Delivery. *IEEE Journal on Flexible Electronics*. **2025** Jul 25.

[15] Wei X, Wang Y, Hu H, Sheng T, Yao Y, Chen C, Xu G, Li K, Su Y, Nan K, Wang J. Wirelessly controlled drug delivery systems for translational medicine. *Nature Reviews Electrical Engineering*. **2025** Mar 25:1-9.

[16] Aschoff A, Kremer P, Hashemi B, Kunze S. The scientific history of hydrocephalus and its treatment. *Neurosurgical review*. **1999** Oct;22(2):67-93.

[17] Shan J, Guo L, Ran P, Zhou Z, Chen J, Chen X, Li J. Implantable double-layer pump chamber piezoelectric valveless micropump with adjustable flow rate function. *Journal of Micromechanics and Microengineering*. **2022** Aug 17;32(10):105002.

[18] Dhwaj A, Roy N, Jaiswar A, Prabhakar A, Verma D. 3D-printed impedance micropump for continuous perfusion of the sample and nutrient medium integrated with a liver-on-chip prototype. *ACS omega*. **2022** Nov 4;7(45):40900-10.

[19] Silverio V, Canane PAG, Martins TA, Afonso R, Cardoso S, Batista E. Development of a microfluidic electroosmosis pump on a chip for steady and continuous fluid delivery. *Biomed Tech (Berl)*. **2022** Dec 19;68(1):79-90. doi: 10.1515/bmt-2022-0051. PMID: 36525637.

[20] Mohith S, Karanth PN, Kulkarni SM. Recent trends in mechanical micropumps and their applications: A review. *Mechatronics*. **2019** Jun 1;60:34-55.

[21] Amirouche F, Zhou Y, Johnson T. Current micropump technologies and their biomedical applications. *Microsystem technologies*. **2009** May;15(5):647-66.

[22] Wang W, Zhang Y, Tian L, Chen X, Liu X. Piezoelectric diffuser/nozzle micropump with double pump chambers. *Frontiers of Mechanical Engineering in China*. **2008** Dec;3(4):449-53.

[23] Woias P. Micropumps: summarizing the first two decades. In *Microfluidics and BioMEMS* **2001** Sep 28 (Vol. 4560, pp. 39-52). SPIE.

[24] Yamahata C, Lotto C, Al-Assaf E, Gijs MA. A PMMA valveless micropump using electromagnetic actuation. *Microfluidics and Nanofluidics*. **2005** Jul;1(3):197-207..

[25] Stemme E, Stemme G. A valveless diffuser/nozzle-based fluid pump.

Just Accepted

Sensors and Actuators A: physical. **1993** Nov 1;39(2):159-67.

[26] Olsson A, Stemme G, Stemme E. The first valve-less diffuser gas pump. In *Proceedings IEEE The Tenth Annual International Workshop on Micro Electro Mechanical Systems. An Investigation of Micro Structures, Sensors, Actuators, Machines and Robots* **1997** Jan 26 (pp. 108-113). IEEE.

[27] A. H. Gibson, Hydraulics and Its Applications, Constable, London, **1945**, p. 93.

[28] Zhang B, Lai BF, Xie R, Davenport Huyer L, Montgomery M, Radisic M. Microfabrication of AngioChip, a biodegradable polymer scaffold with microfluidic vasculature. *Nature protocols*. **2018** Aug;13(8):1793-813.

[29] Tran RT, Thevenot P, Gyawali D, Chiao JC, Tang L, Yang J. Synthesis and characterization of a biodegradable elastomer featuring a dual crosslinking mechanism. *Soft matter*. **2010**;6(11):2449-61.

[30] Rotundo S, Brizi D, Flori A, Giovannetti G, Menichetti L, Monorchio A. Shaping and focusing magnetic field in the human body: State-of-the art and promising technologies. *Sensors*. **2022** Jul 8;22(14):5132.

[31] Sant'Ovaia H, Marques G, Santos A, Gomes C, Rocha A. Magnetic susceptibility and isothermal remanent magnetization in human tissues: a study case. Biometals. 2015 Dec;28(6):951-8.

[32] Schenck JF. Safety of strong, static magnetic fields. Journal of magnetic resonance imaging. 2000 Jul;12(1):2-19.

[33] Talagala SL, Lowe IJ. Introduction to magnetic resonance imaging. Concepts in Magnetic Resonance. 1991 Jul;3(3):145-59.

[34] Van Geuns RJ, Wielopolski PA, de Bruin HG, Rensing BJ, Van Ooijen PM, Hulshoff M, Oudkerk M, de Feyter PJ. Basic principles of magnetic resonance imaging. Progress in cardiovascular diseases. 1999 Sep 1;42(2):149-56.

[35] Obaidat IM, Narayanaswamy V, Alaabed S, Sambasivam S, Muralee Gopi CV. Principles of magnetic hyperthermia: a focus on using multifunctional hybrid magnetic nanoparticles. Magnetochemistry. 2019 Dec 6;5(4):67.

[36] Etli Omur E, Akar A. Magnetic nanoparticles for diagnosis and treatment. Medicine Science. 2022;11(2).

[37] Gilchrist RK, Medal R, Shorey WD, Hanselman RC, Parrott JC, Taylor CB. Selective inductive heating of lymph nodes. Annals of surgery. 1957 Oct 1;146(4):596-606.

[38] Guo R, Zhang L, Chen H, Du H, Qu Z, Zhang X. Magnetic Properties of Biological Samples. InBiological Effects of Static Magnetic Fields 2023 Feb 22 (pp. 49-74). Singapore: Springer Nature Singapore.

[39] Taylor DS. The magnetic properties of myoglobin and ferrimyoglobin, and their bearing on the problem of the existence of magnetic interactions in hemoglobin. Journal of the American Chemical Society. 1939 Aug;61(8):2150-4.

[40] Taylor DS, Coryell CD. The magnetic susceptibility of the iron in ferrohemoglobin. Journal of the American Chemical Society. 1938 May;60(5):1177-81.

[41] Choi Y, Koo J, Rogers JA. Inorganic materials for transient electronics in biomedical applications. *MRS Bulletin*. **2020** Feb;45(2):103-12.

[42] Spotnitz WD. Fibrin sealant: the only approved hemostat, sealant, and adhesive—a laboratory and clinical perspective. *International scholarly research notices*. **2014**;2014(1):203943.

[43] C. M. Boutry, B. C. Schroeder, Z. Bao, A. Legrand, P. Fox, *Proc. IEEE Biomed. Circuits Syst. Conf. (BioCAS)*, **2016**, 144–147.

[44] Boutry CM, Schroeder BC, Bao Z, Legrand A, Fox P. A sensor measuring deformation and pressure, entirely biodegradable, for orthopedic applications. *In 2016 IEEE Biomedical Circuits and Systems Conference (BioCAS)* **2016** Oct 17 (pp. 144-147). IEEE.

[45] Faivre M, Gelszinnis R, Degouttes J, Terrier N, Riviere C, Ferrigno R, Deman AL. Magnetophoretic manipulation in microsystem using carbonyl iron-polydimethylsiloxane microstructures. *Biomicrofluidics*. **2014** Sep 1;8(5).

[46] Barker DE. Skin thickness in the human. *Plastic and Reconstructive Surgery*. **1951** Feb 1;7(2):115-6.

[47] Fung YC. Biomechanics: mechanical properties of living tissues. Springer Science & Business Media; 2013 Mar 14.

[48] Greene PR. Electrical analogs for Kelvin & Maxwell viscoelastic materials: Applications to cornea & sclera. New Frontiers Ophthalmology, Oatxt. 2017 Jan 1.

[49] Morganti E, Fuduli I, Montefusco A, Petasecca M, U. Pignatel* G. SPICE modelling and design optimization of micropumps. *International Journal of Environmental Analytical Chemistry*. **2005** Aug 10;85(9-11):687-98.

[50] Bourouina T, Grandchamp JP. *Modeling micropumps with electrical equivalent networks. Journal of Micromechanics and Microengineering.* **1996** Dec 1;6(4):398.

[51] Ullmann A, Fono I. The piezoelectric valve-less pump-improved dynamic model. *Journal of Microelectromechanical systems*. **2002** Dec 31;11(6):655-64.

[52] e Lima KM, Júnior JF, de Albuquerque Pereira WC, de Oliveira LF. Assessment of the mechanical properties of the muscle-tendon unit by supersonic shear wave imaging elastography: a review. Ultrasonography. 2018 Jan 1;37(1):3-15.

[53] Cortes DH, Suydam SM, Silbernagel KG, Buchanan TS, Elliott DM. Continuous shear wave elastography: a new method to measure viscoelastic properties of tendons *in vivo*. Ultrasound in medicine & biology. 2015 Jun 1;41(6):1518-29.

© The Author(s) 2026. *Nano Research* published by Tsinghua University Press. The articles published in this open access journal are distributed under the terms of the Creative Commons Attribution 4.0 International License (http://creativecommons.org/licenses/by/4.0/), which permits use, distribution and reproduction in any medium, provided the original work is properly cited.

Just Accepted

Electronic Supplementary Material

A biodegradable implantable micropump for biomedical applications, focusing on peripheral nerve repair

Elena Aprea[1], Feyza Pirim-Aslan[1], Francesco Stallone[2], Vasiliki Gkouzioti[3], Zhengwei Liao[1], Leon Abelmann[1], Jean-Philippe Frimat[3], Pasqualina M. Sarro[1], and Clementine M. Boutry[1]

[1] *Department of Microelectronics, Delft University of Technology, 2628 CD Delft, the Netherlands*
[2] *Else Kooi Laboratory, Delft University of Technology, 2628 CD Delft, the Netherlands*
[3] *Department of Neurology and Department of Human Genetics, Leiden University Medical Center, 2333 ZC Leiden, the Netherlands*

Supporting information to https://doi.org/10.26599/NR.2026.94908590

Just Accepted

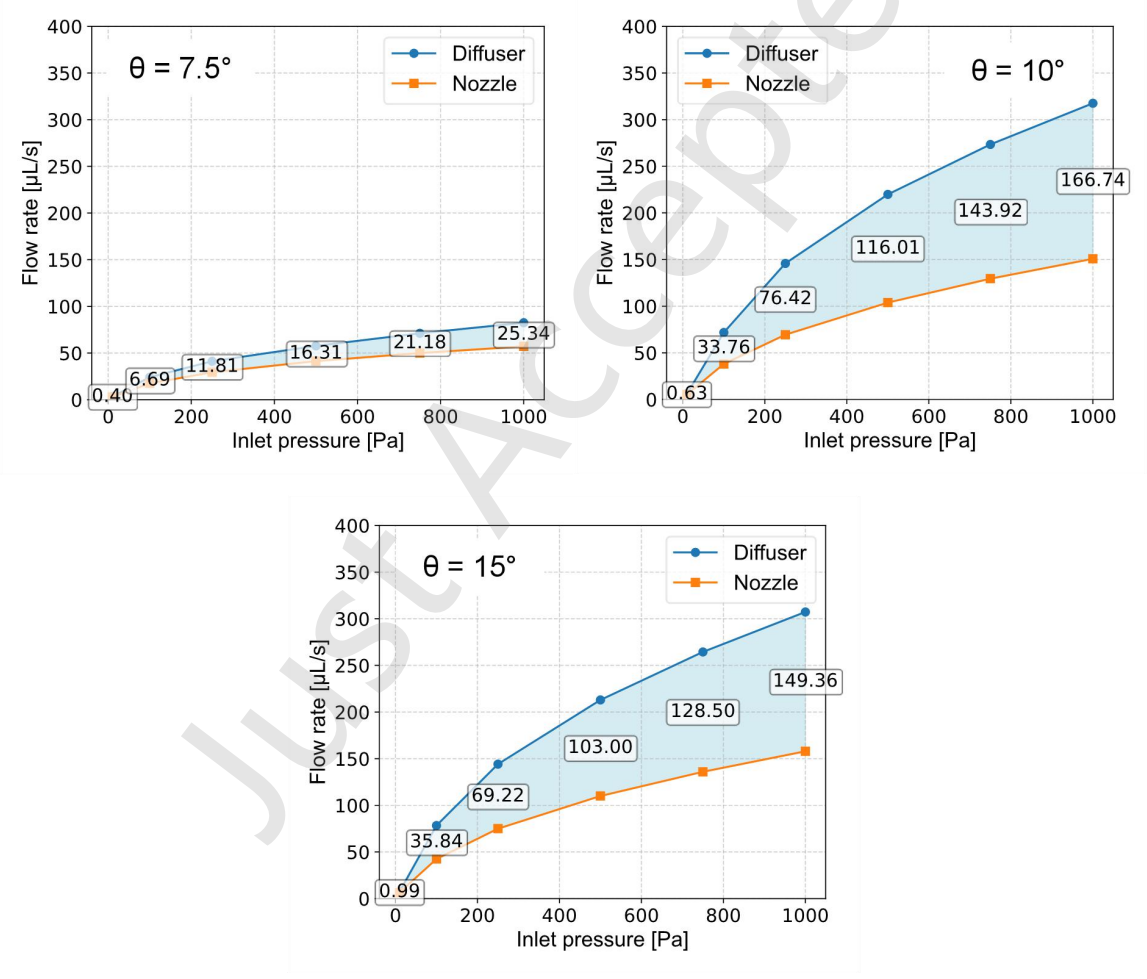


Figure S1. Net flow rate comparison in nozzle/diffuser geometry simulated in COMSOL Multiphysics. The graphs present the flow rate for various pressure differences applied at the inlet (0 to 1000 Pa). The geometry of nozzle and diffuser is obtained by switching the inlet and outlet in the two configurations. The nozzles/diffusers are characterized by three angles: $\theta = 7.5, 10,$ and $15°$. The net flow rate is shaded in blue, and it is maximized for angles $\theta \approx 10°$.

Address correspondence to c.m.f.viellard-boutry@tudelft.nl

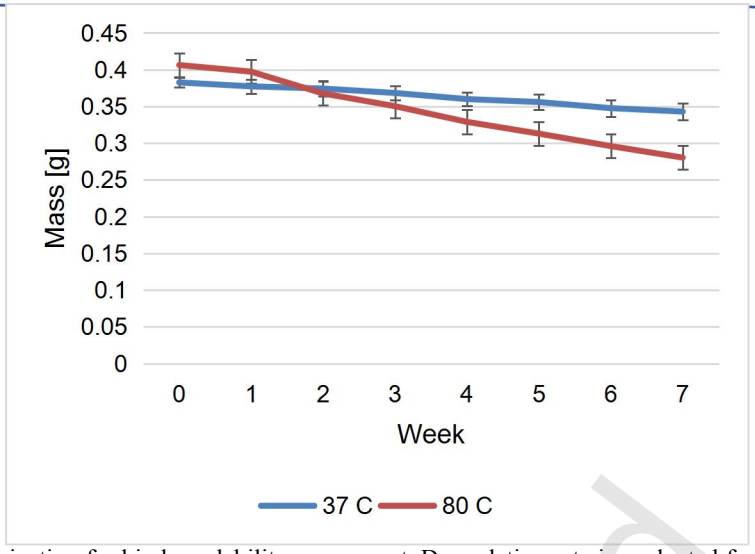
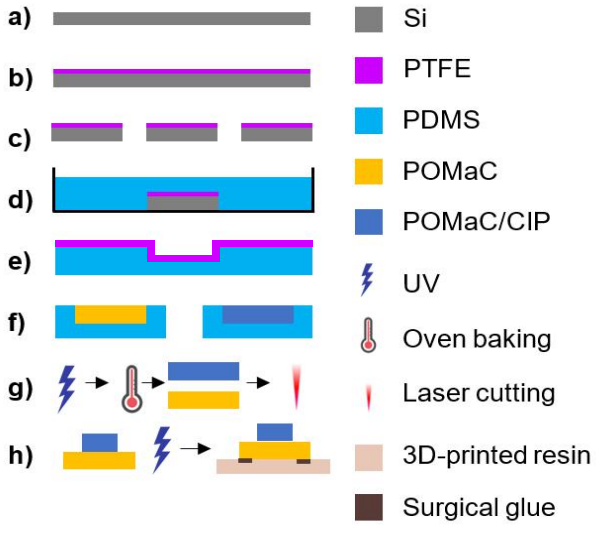


Figure S2. Mass loss characterization for biodegradability assessment. Degradation rate is evaluated for devices immersed in PBS (pH 7.4) at 37 and 80 °C to show regular and accelerated degradation. Each week, n=3 devices are retrieved from PBS, dried under nitrogen flow and weighed. After 7 weeks, the degradation rate is calculated and averaged, resulting in 5.6 mg/week and 18 mg/week, respectively.



Figure S3. POMaC Synthesis main steps. a) Mixing 1,8 octanediol, citric acid, and maleic anhydride (5:1:4) at 140 °C for 3 hours under nitrogen flow. b) Cooling down to 100 °C, adding 1-4 dioxane and performing a purification step through a separatory funnel, precipitating the solution into deionized water. c) Water is poured away, pre-POMaC is collected and dried overnight under nitrogen flow.



Just Accepted

Figure S4. Membrane fabrication process (POMaC and POMaC/CIP micro-molding). a) A 500 µm-thick Si wafer was coated with b) a layer of 180 nm of PECVD deposited PTFE used as anti-adhesion layer. The wafer was then c) saw-diced in 2x2 cm² parts and d) it was employed as master mold to obtain e) a 10:1 (base:curing agent) PDMS negative mold with a 500 µm-deep structure. The negative mold was once again coated with a layer of 180 nm of PECVD deposited PTFE used as anti-adhesion layer. POMaC and POMaC/CIP were subsequently f) cast in the molds, then g) UV crosslinked and oven-baked according to the protocol time. They were finally released, washed in PBS and laser cut. The obtained shapes were h) UV bonded to each other and assembled with the 3D-printed resin through surgical glue.

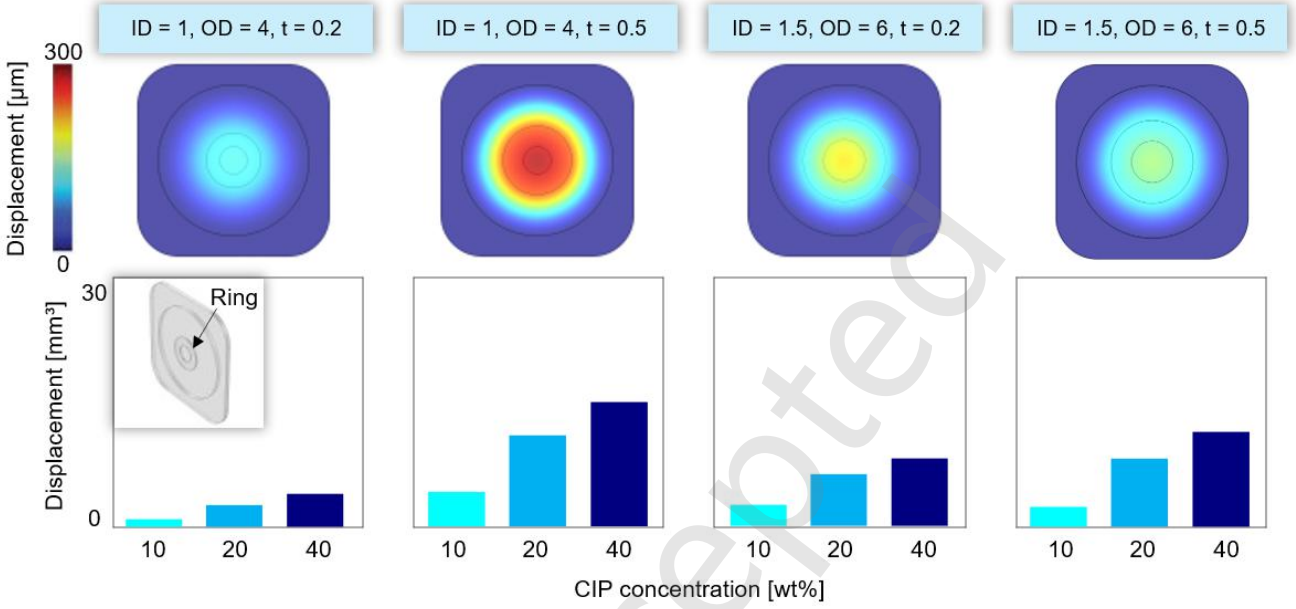


Figure S5. COMSOL Multiphysics analysis for the ring configuration (*OD:ID* = 4:1 or 6:1.5); core-shaped membranes reported in Figure 4 outperform ring-shaped ones.

Just Accepted

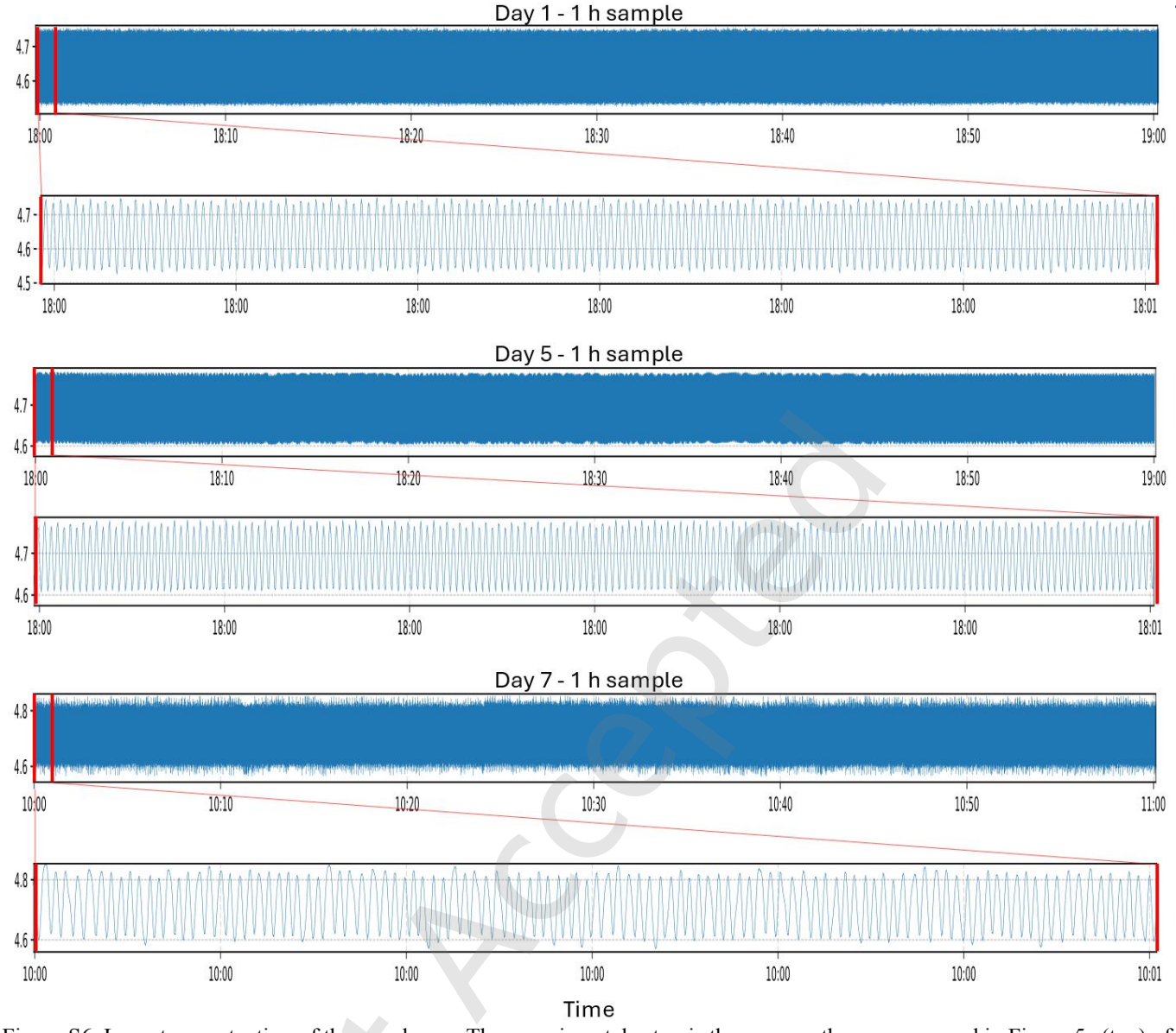


Figure S6. Long-term actuation of the membrane. The experimental setup is the same as the one proposed in Figure 5a (top) of the manuscript. The experiment was run for a total of 1 week. Three segments of the recording are displayed: the first one at the beginning of the recording on day 1, the second on day 5, and the last one on day 7. A zoom on one minute of each recording segment is also reported, to allow the visualization of the plot details. The amplitude of the oscillation remains coherent throughout the measurement (220 ± 30 μm).

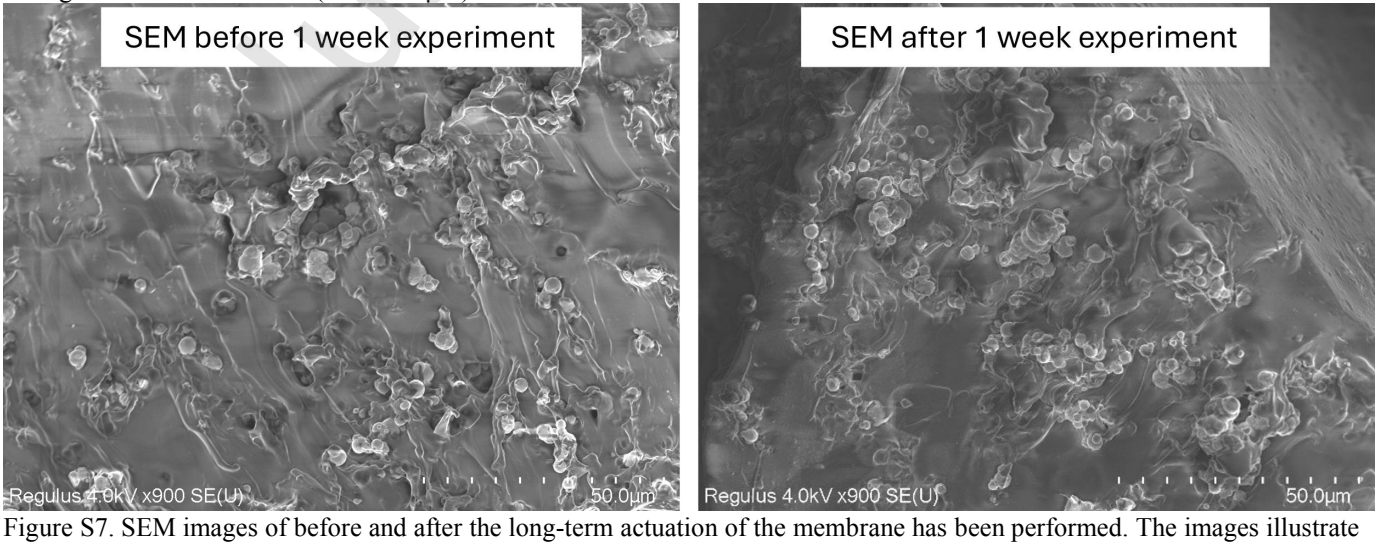


Figure S7. SEM images of before and after the long-term actuation of the membrane has been performed. The images illustrate the cross-section of the POMaC/CIP membrane element. No significant differences are observed between the two conditions, indicating that no damage is present.

Just Accepted

Table ST1. Micropump dimensions and relevant design parameters.

Element name	Acronym	Value
Membrane edge	l_{POMaC}	5 mm
Membrane thickness	h_{POMaC}	0.5 mm
Cosinusoidal flexion	γ	0.297
Young's modulus POMaC	E_{POMaC}	19 kPa
Poisson's ratio POMaC	ν_{POMaC}	0.49
Density POMaC	ρ_{POMaC}	725 kg m^{-3}
Density POMaC/CIP	$\rho_{POMaC/CIP}$	1631.7 kg m^{-3}
POMaC/CIP radius	$r_{POMaC/CIP}$	3 mm
POMaC/CIP thickness	$h_{POMaC/CIP}$	0.5 mm
Chamber depth	h_C	0.6 mm
Chamber radius	r_C	4 mm
Glue reservoir depth	h_g	0.1 mm
Glue reservoir inner diameter	d_g	10 mm
Valves efficiency	ε	0.066
Valves length	l_v	1130 µm
Valves minimum width	α_{min}	100 µm
Valves max width	α_{max}	500 µm
Valve width at x location	2α	$\alpha = [(\alpha_{max} - \alpha_{min})/2*l_v]*x + \alpha_{min}/2$ (µm)
Valve height	b	50 µm
Channel length	l_t	3.514 mm
Channel diameter	d_c	100 µm
Channel width	$2\alpha_t$	100 µm
Channel height	$2b_t$	100 µm
Tube length (inlet)	$l_{p,c}$	60 mm
Tube inner radius (inlet)	$r_{p,c}$	0.8 mm
Tube length (outlet)	$l_{t,o}$	80 mm
Tube inner radius (outlet)	$r_{t,o}$	10 mm
Tissue Young's Modulus [52]	E_{tissue}	50 kPa
Tissue viscosity [53]	η_{tissue}	35 Pa*s

Just Accepted

Tissue radius	r_{tissue}	0.75 mm
Tissue (virtual) length (per side of the T-shaped conduit)	l_{tissue}	50 cm

Table ST2. Core and ring membrane configurations and relative dimensions of the magnetic element.

Configuration	Inner Diameter (ID) [mm]	Outer Diameter (OD) [mm]	Thickness [mm]
Core 1	-	4	0.2
Core 2	-	4	0.5
Core 3	-	6	0.2
Core 4	-	6	0.5
Ring 1	1	4	0.2
Ring 2	1	4	0.5
Ring 3	1.5	6	0.2
Ring 4	1.5	6	0.5

Table ST3. Values for equivalent circuit. The values are calculated according to literature [49-51], the parameters used in the formulas are listed in ST1.

Element name	Acronym	Value
Hydraulic resistance, channel	$R_{channel}$	2.1 e10 Ns m^{-5}
Hydraulic resistance, tube	R_{tube}	1.4 e9 Ns m^{-5}
Hydraulic inductance, channel	$L_{channel}$	5.3 e5 Ns^2 m^{-5}
Hydraulic inductance, tube	L_{tube}	2.4 e4 Ns^2 m^{-5}
Hydraulic capacitance, channel	$C_{channel}$	2.0 e-16 m^6 J^{-1}
Hydraulic capacitance, tube	C_{tube}	3.8 e-14 m^6 J^{-1}
Hydraulic resistance, diffuser	$R_{diffuser,in}$/ $R_{diffuser,out}$	9.5 e4 Ns m^{-5}
Hydraulic resistance, nozzle	$R_{nozzle,in}$/ $R_{nozzle,out}$	1.4 e5 Ns m^{-5}
Hydraulic inductance, diffuser	$L_{diffuser,in}$/ $L_{diffuser,out}$	3.7 e5 Ns^2 m^{-5}
Hydraulic inductance, nozzle	$L_{nozzle,in}$/ $L_{nozzle,out}$	5.3 e5 Ns^2 m^{-5}
Hydraulic resistance, outlet	R_{out}	18.49 Ns m^{-5}
Hydraulic capacitance, outlet	C_{out}	7.17 e-10 m^6 J^{-1}
Hydraulic inductance, outlet	L_{out}	75.4 Ns^2 m^{-5}
Equivalent resistance, tissue	R_{tissue}	2.0 e7 Ns m^{-5}
Equivalent capacitance, tissue	C_{tissue}	4 e-11 m^6 J^{-1}

Just Accepted

The equivalent inductances, resistances and capacitances in the tissue-tube-channel part of the circuit have been scaled by a factor $s = 10^5$ to maintain coherence with measurement units in LT Spice.

Chamber pressure drop calculation:

The pressure drop inside the chamber due to membrane upward displacement of Δx is given by the following calculations.

Initial volume of the chamber:

$V_0 = \pi \cdot r_c^2 \cdot h_c = \pi \cdot (0.004\ m)^2 \cdot (0.0006\ m) = 3.02\ e\text{-}8\ m^3$

Membrane diameter: $d \approx 10\ mm = 0.01\ m$

Membrane area:

$A = (\pi \cdot d^2)/4 = (\pi \cdot (0.01\ m)^2)/4 = 7.854\ e\text{-}5\ m^2$

Membrane displacement upwards: $\Delta x = +250\ \mu m = 2.5\ e\text{-}4\ m$

Additional volume due to membrane lift:

$\Delta V = A \cdot \Delta x = 7.854\ e\text{-}5\ m^2 \cdot 2.5 \times 10^{-4}\ m = 1.964\ e\text{-}8\ m^3$

Final volume:

$V = V_0 + \Delta V = 3.02\ e\text{-}8\ m^3 + 1.964\ e\text{-}8\ m^3 = 4.984\ e\text{-}8\ m^3$

Assuming an adiabatic process:

$P \cdot V^x = constant \rightarrow P = P_0 \cdot (V_0 / V)^x$

Where:

$P_0 = 101{,}300\ Pa$ (initial pressure)

$x = 1.4$ (adiabatic index for air)

$V_0 = 3.02\ e\text{-}8\ m^3$

$V = 4.984\ e\text{-}8\ m^3$

$V_0 / V = 0.606$

$P = 101{,}300 \cdot (0.606)^{1.4} \approx 101300 \cdot 0.482 = 48{,}870\ Pa$

When the membrane moves upward by 250 µm, the volume increases and the gas pressure drops from 101.3 kPa to approximately 48.9 kPa (assuming an adiabatic process).

Equivalent resistance and capacitance modeling for the tissue:

The inlet tube is linked to an equivalent circuit representing the tissue. Tissue values for Young's Modulus and viscosity are taken from literature [52, 53]. The circuit captures the viscoelastic behavior of human nerves, based on geometrical parameters corresponding to an average nerve (diameter: 1.5 mm; effective length approximated to 50 cm per side of the tube). The nerve's mechanical behavior is modeled using a Kelvin–Voigt viscoelastic analogy to electrical circuits. The analogies and calculations are reported below.

Table ST4: Kelvin–Voigt viscoelastic analogy to circuit, where the equivalent resistance accounts for viscous damping (analogous to viscosity), and the equivalent capacitance represents the reciprocal of elastic stiffness (analogous to the Young's Modulus).

Material property	**Mechanical Equivalent**	**Electrical Equivalent**
Young's Modulus (E)	Spring constant (k)	Capacitance ($C \propto 1/k$)
Viscosity (η)	Damping coefficient (c)	Resistance ($R \propto c$)

Spring constant: $k = \frac{EA}{L}$, where E is the Young's Modulus of the tissue, A is the cross-sectional area and L is the virtual length of the nerve.

Damping coefficient: $c = \frac{\eta A}{L}$, where η is the viscosity of the tissue.

The equivalent capacitance and resistance are scaled by the square of the tissue cross-sectional area.

$C = \frac{A^2}{k}$, where k is the spring constant.

$R = \frac{c}{A^2}$, where c is the damping coefficient.

Just Accepted